

# Water mass analysis of the 2018 US GEOTRACES Pacific Meridional Transect (GP15)

Rian M Lawrence<sup>1</sup>, Avanti Shrikumar<sup>1</sup>, Emilie Le Roy<sup>2</sup>, James H. Swift<sup>3</sup>, Phoebe J. Lam<sup>4</sup>, Gregory Cutter<sup>5</sup>, and Karen L Casciotti<sup>6</sup>

<sup>1</sup>Stanford University

<sup>2</sup>Woods Hole Oceanographic Institution

<sup>3</sup>Scripps Institution of Oceanography

<sup>4</sup>University of California, Santa Cruz

<sup>5</sup>Old Dominion University

<sup>6</sup>Stanford University, Department of Environmental Earth System Science

November 21, 2022

## Abstract

A water mass analysis is a tool for interpreting the effect of ocean mixing on the distributions of trace elements and isotopes (TEI's) along an oceanographic transect. The GEOTRACES GP15 transect along 152°W covers a wide range in latitude from Alaska to Tahiti. Our objective is to present the nutrients and hydrography of GP15 and quantify the distributions of water masses to support our understanding of TEI distributions along GP15. We used a modified Optimum Multiparameter (OMP) analysis to determine the distributions of water masses with high importance to nutrient and hydrographic features in the region. In the thermocline, our results indicated the dominance of Pacific Subarctic Upper Water (PSUW) in the subpolar gyre, Eastern North Pacific Central Water (ENPCW) in the northern subpolar gyre, and Equatorial Subsurface Water (ESSW) in the equatorial region. South Pacific Subtropical Water (SPSTW) dominated the top of the thermocline in the southern subtropical gyre, while South Pacific Central Water (SPCW) dominated the lower thermocline. Antarctic Intermediate Water (AAIW), Equatorial Intermediate Water (EqIW), and North Pacific Intermediate Water (NPIW) in the southern hemisphere, equatorial region, and northern hemisphere, respectively, occupied waters just below the thermocline. Dominant water masses in the deep waters of the southern hemisphere include Upper Circumpolar Deep Water (UCDW) and Lower Circumpolar Deep Water (LCDW) with minimal contributions from Antarctic Bottom Water (AABW). Pacific Deep Water (PDW) dominated the deep water in the northern hemisphere. Our results align well with literature descriptions of these water masses and related circulation patterns.

1           **Water mass analysis of the 2018 US GEOTRACES**  
2           **Pacific Meridional Transect (GP15)**

3           **R. M. Lawrence**<sup>1</sup>, **A. Shrikumar**<sup>1</sup>, **E. Le Roy**<sup>2</sup>, **J. Swift**<sup>3</sup>, **P. J. Lam**<sup>4</sup>, **G.**  
4           **Cutter**<sup>5</sup>, and **K. L. Casciotti**<sup>1</sup>

5                           <sup>1</sup>Department of Earth System Science, Stanford University, Stanford, CA, USA

6           <sup>2</sup>Department of Marine Chemistry and Geochemistry, Woods Hole Oceanographic Institution, Woods  
7                           Hole, MA, USA

8           <sup>3</sup>Department of Climate, Atmospheric Science, and Physical Oceanography, Scripps Institution of  
9                           Oceanography, La Jolla, CA 92037, USA

10          <sup>4</sup>University of California, Santa Cruz, Department of Ocean Sciences, 1156 High St, Santa Cruz, CA  
11                           95064, USA

12          <sup>5</sup>Department of Ocean and Earth Sciences, Old Dominion University, Norfolk, VA 23529, USA

13           **Key Points:**

- 14           • We present the hydrography, nutrients, and water mass analysis results for the 2018  
15           GEOTRACES GP15 section.
- 16           • Our modified water mass analysis methodology resulted in similar or lower resid-  
17           uals compared to past water mass analyses.
- 18           • These water mass analysis results will be useful tools for the interpretation of trace  
19           elements and isotopes (TEI's) along GP15.

---

Corresponding author: Rian Lawrence, [rian@stanford.edu](mailto:rian@stanford.edu)

## Abstract

A water mass analysis is a tool for interpreting the effect of ocean mixing on the distributions of trace elements and isotopes (TEI's) along an oceanographic transect. The GEOTRACES GP15 transect along 152°W covers a wide range in latitude from Alaska to Tahiti. Our objective is to present the nutrients and hydrography of GP15 and quantify the distributions of water masses to support our understanding of TEI distributions along GP15. We used a modified Optimum Multiparameter (OMP) analysis to determine the distributions of water masses with high importance to nutrient and hydrographic features in the region. In the thermocline, our results indicated the dominance of Pacific Subarctic Upper Water (PSUW) in the subpolar gyre, Eastern North Pacific Central Water (ENPCW) in the northern subpolar gyre, and Equatorial Subsurface Water (ESSW) in the equatorial region. South Pacific Subtropical Water (SPSTW) dominated the top of the thermocline in the southern subtropical gyre, while South Pacific Central Water (SPCW) dominated the lower thermocline. Antarctic Intermediate Water (AAIW), Equatorial Intermediate Water (EqIW), and North Pacific Intermediate Water (NPIW) in the southern hemisphere, equatorial region, and northern hemisphere, respectively, occupied waters just below the thermocline. Dominant water masses in the deep waters of the southern hemisphere include Upper Circumpolar Deep Water (UCDW) and Lower Circumpolar Deep Water (LCDW) with minimal contributions from Antarctic Bottom Water (AABW). Pacific Deep Water (PDW) dominated the deep water in the northern hemisphere. Our results align well with literature descriptions of these water masses and related circulation patterns.

## Plain Language Summary

This paper describes the measured water properties, such as temperature, salinity, and nutrients, and the ocean water mixing ratios derived from them, at depths sampled on a line between Alaska and Tahiti. We identified the water masses containing distinctive water properties found in this geographic area. Properties of these water masses were used to determine the theoretical contributions of each water mass to our ocean water samples. Using this information, we can determine if chemical concentrations and forms found in each sample can be explained by water mixing alone, or if additional chemical changes have occurred. Our water mass mixing results illustrate where nutrients have been regenerated in the water column, and largely align with past studies' results; however, our error is lower than in some past studies.

## 1 Introduction

Expected trace element and isotope (TEI) distributions from water mass mixing are determined via a water mass analysis. For example, Roshan and Wu (2015) identified water mass mixing, rather than another process such as regeneration, as the primary modulator of North Atlantic zinc distributions based on the water mass analysis results of Jenkins et al. (2015). Evans et al. (2020) used their water mass analysis results to investigate the Eastern Tropical North Pacific, an area of interest due to its oxygen deficient zone. Their results showed the secondary nitrite maximum is confined to a water mass with an oxygen concentration so low nitrate becomes the primary oxidant. They also compared distributions of iodine species to their water mass analysis results to identify possible water masses sources of redox species besides nitrite (Evans et al., 2020). Peters, Lam, and Casciotti (2018) used the water mass results of Peters, Jenkins, et al. (2018) to calculate the expected nitrate ( $\text{NO}_3^-$ ) concentration and its isotopic composition of the cruise samples. This calculated expected nitrate was compared to the actual cruise measurements to estimate how much nitrate regeneration occurred to make up for any discrepancy. In sum, results from water mass analyses have proven helpful

69 for the interpretation of many TEI's (Le Roy et al., 2018; Artigue et al., 2021; Deng et  
70 al., 2018).

71 The 2018 GEOTRACES GP15 transect followed 152°W from Alaska to Tahiti; a  
72 transect carefully planned by the GEOTRACES program to optimize its relevance to  
73 understanding the sources, sinks, and internal cycling of TEI's (GEOTRACES Science  
74 Planning Group, 2006). The distribution of TEI's on GP15 are thought to be influenced  
75 by the Aleutian margin, hydrothermal plumes, oxygen deficient zones (ODZ's), and dif-  
76 fering surface ocean biogeography. The Aleutian margin is a possible boundary source  
77 of elements such as iron, silicate, and rare earth elements while likely also a boundary  
78 sink with high rates of particle scavenging in its deep waters (Lam et al., 2006; Hu et  
79 al., 2014; Hautala & Hammond, 2020; Haley et al., 2014, 2014). GP15 is also impacted  
80 by hydrothermal plumes, namely the East Pacific Rise (EPR), Loihi Seamount, and Juan  
81 de Fuca Ridge (JdFR) (Mahoney et al., 1994; Sedwick et al., 1992; Trefry et al., 1994).  
82 These are sources of trace elements; for example, the Loihi Seamount is a significant source  
83 of iron in the North Pacific (Jenkins et al., 2020). Signals from the the oxygen deficient  
84 zone of the Eastern Tropical Pacific are also seen along GP15. ODZ's are generally known  
85 to be a sink of fixed nitrogen, a source of nitrous oxide, and have characteristic nutri-  
86 ent and trace metal characteristics (Chang et al., 2012; Yamagishi et al., 2007; Nameroff  
87 et al., 2002). Volcanic strata surrounds the Pacific basin (the "ring of fire"), and TEI's  
88 released from the strata may be tracked by neodymium isotopes (Amakawa et al., 2004).

89 In addition these features, the transect also covers a wide range in surface biolog-  
90 ical regimes. GP15 transits the high-nutrient, low-chlorophyll (HNLC) conditions in the  
91 eastern subarctic Pacific, passes through the oligotrophic North Pacific subtropical gyre,  
92 crosses the HNLC conditions at the equator, and ends in some of the most oligotrophic  
93 waters in the world's oceans in the South Pacific gyre. Circulation features traversed in-  
94 clude the Alaskan Gyre, the Pacific subtropical gyres, and the complex Pacific equato-  
95 rial current system (Talley, 2011). GP15 also transects the ocean's oldest deep waters  
96 with low oxygen and high levels of regenerated nutrients (Hautala & Hammond, 2020;  
97 Holzer et al., 2021). TEI's can be compared across these regimes to better constrain up-  
98 take, scavenging, export, and regeneration. GP15 adds to GEOTRACES' growing net-  
99 work of basin-scale transects and contributes towards GEOTRACES's objectives of doc-  
100 umenting TEI's and understanding TEI's physical and biological controls (Measures et  
101 al., 2007; GEOTRACES Science Planning Group, 2006). Here we describe the nutrients  
102 and hydrography measured on GP15, relating them qualitatively and quantitatively to  
103 water mass distributions in the region. A modified Optimum Multiparameter (OMP)  
104 analysis was employed to determine water mass fractions in GP15 samples (Shrikumar  
105 et al., 2022). The work presented here provides water mass and circulation context for  
106 GP15, a foundation needed to align to GEOTRACES's objectives at the basin-scale and  
107 beyond.

## 108 2 Methods

### 109 2.1 Cruise information and relevant measurements

110 The GEOTRACES Pacific Meridional Transect, GP15, was conducted on R/V Roger  
111 Revelle along 152°W (except for the first five stations off the coast of Alaska) from 18  
112 September to 24 November 2018. The Oceanographic Data Facility (ODF, Scripps In-  
113 stititution of Oceanography) collected temperature, and salinity, dissolved oxygen, and  
114 nutrient measurements using standard methods described in the GP15 cruise report and  
115 GO-SHIP best practices (Cutter et al., 2018; Becker et al., 2020). Briefly, nitrate ( $\mu\text{mol}$   
116  $\text{kg}^{-1}$ ), silicate ( $\mu\text{mol kg}^{-1}$ ), and phosphate ( $\mu\text{mol kg}^{-1}$ ) concentrations were measured  
117 on board after allowing sample bottles to come to room temperature over 2-12 hours.  
118 Dissolved oxygen samples were analyzed on board within 2-14 hours of collection and  
119 were also used to calibrate measurements taken via CTD sensor (Sea-Bird Electronics

120 *9plus*/ SBE9+). Data were flagged according to the SeaDataNet scheme as is recommended  
121 by GEOTRACES (SeaDataNet, 2010; GEOTRACES, n.d.). The GP15 bottle and ODF  
122 CTD data can be found on the Biological and Chemical Oceanography Data Manage-  
123 ment Office (BCO-DMO) website (Cutter et al., 2021a, 2021b, 2020) and in the 2021 GEO-  
124 TRACES Intermediate Data Product (GEOTRACES Intermediate Data Product Group,  
125 2021). Only samples from the ODF rosette, with complete data collected by ODF and  
126 without any data flagged as a known bad value were used for the analysis.

## 127 2.2 Water mass analysis

128 The Optimum Multiparameter (OMP) analysis was conducted using the Python  
129 package, *pyompa* (Shrikumar et al., 2022). *pyompa* contains code adapted from Peters,  
130 Jenkins, et al. (2018) and Jenkins et al. (2015). Details about the *pyompa* package, OMP  
131 method, and the *pyompa* modifications to previous implementations of the OMP method  
132 can be found in Shrikumar et al. (2022). In brief, the OMP is a system of linear equa-  
133 tions solved via weighted least-squares for water mass fractions of each defined water type  
134 in a sample (Tomczak, 1981). Key method modifications for this GP15 implementation  
135 are discussed below. The *pyompa* software can be found in Zenodo ([https://zenodo](https://zenodo.org/record/5733887)  
136 [.org/record/5733887](https://zenodo.org/record/5733887)), and the code to replicate the analysis can be found in Github  
137 (<https://github.com/nitrogenlab/gp15wmscripts>).

### 138 2.2.1 Analysis structure

139 The water mass analysis for GP15 was divided into two analyses; one for the ther-  
140mocline and the other for intermediate and deep waters. The thermocline analysis was  
141 kept separate to account for the impact of the thermocline’s stratification on water mass  
142 mixing. Water masses in the thermocline were restricted to mixing along isopycnals, while  
143 the intermediate and deep water mass analysis allows some diapycnal mixing. Details  
144 are discussed further below. Previous iterations of the OMP method also divided inter-  
145 mediate and deep waters into separate analyses (Jenkins et al., 2015; Peters, Jenkins,  
146 et al., 2018). The reason for this was twofold; 1) this kept deep water masses out of in-  
147 termediate depths and vice versa, and 2) this increased the number of water masses that  
148 could be included while maintaining a fully-determined solution.

149 We were able to circumvent the first issue by implementing soft penalties (see Ta-  
150 bles 1, 2, and Text S1). Soft penalties were set at the  $\sigma_0$  and/or latitudinal limits of a  
151 water mass reported in the literature. The soft penalty penalized use of a given water  
152 mass starting at its limits, and increased the penalty the farther a sample was past the  
153 limit. This technique was used to restrict water masses to observed  $\sigma_0$  ranges, as well  
154 as certain latitudes; for example, a northern water mass can be penalized from being uti-  
155 lized in the south.

156 The number of water masses used in prior analyses was constrained to be less than  
157 or equal to the number of parameters, or water mass properties, used in the analysis to  
158 obtain a fully-determined solution. By separating an oceanographic transect into regional  
159 analyses, prior studies were able to include the water masses needed to define their tran-  
160 sect. Here, we were able to include more water masses than the number of parameters  
161 by using penalties, as described above, but also by using results of an ocean circulation  
162 model (OCIM) to constrain our results to a single solution (Holzer et al., 2021; Shriku-  
163 mar et al., 2022).

164 The OCIM model was run with the same regional water mass definitions as the OMP  
165 analysis. The OMP was then constrained to select the solution, out of a number of equiv-  
166 alent solutions, that yields the water mass distribution closest to the OCIM model re-  
167 sults. Please see Shrikumar et al. (2022) for further explanation of this method. For our  
168 OCIM-constrained OMP analysis solution, the solver did not converge on a solution for

169 17 of the samples. In other words, the solver didn't find a solution similar to the OCIM  
 170 results with the same residuals as the unconstrained OMP analysis. However, we report  
 171 solutions for these 17 samples meeting the standard residuals requirements from our OMP  
 172 solver.

### 173 **2.2.2 Parameters and Weighting**

174 The properties used to define water types, as well as the sample parameters used  
 175 in the analysis, included conservative temperature ( $^{\circ}\text{C}$ ), absolute salinity, silicate  $[\text{Si}(\text{OH})_4]$   
 176 ( $\mu\text{mol kg}^{-1}$ ), dissolved oxygen  $[\text{O}_2]$  ( $\mu\text{mol kg}^{-1}$ ), phosphate  $[\text{PO}_4^{3-}]$  ( $\mu\text{mol kg}^{-1}$ ), and  
 177 nitrate  $[\text{NO}_3^-]$  ( $\mu\text{mol kg}^{-1}$ ). Absolute salinity and conservative temperature data were  
 178 computed from the CTD data using the Python implementation of the Gibbs Sea Wa-  
 179 ter Oceanographic Toolbox of TEOS-10 (<https://teos-10.github.io/GSW-Python/>),  
 180 while the other parameters were measured in sample bottles, as described above.

181 For the water mass analyses, we used a different set of parameter weights for the  
 182 thermocline analysis than the intermediate and deep water analysis (Section 2.2.1) as  
 183 in Peters, Jenkins, et al. (2018). The weights applied to the thermocline OMP analy-  
 184 sis were 20.0, 15.5, 0.5, 5, 5, and 1 for conservative temperature, salinity,  $\text{Si}(\text{OH})_4$ ,  $\text{NO}_3^-$ ,  
 185  $\text{PO}_4^{3-}$ , and  $\text{O}_2$ , respectively. The intermediate and deep OMP analysis weights were of  
 186 56, 80, 3, 5, 5, and 1 for conservative temperature, salinity,  $\text{Si}(\text{OH})_4$ ,  $\text{NO}_3^-$ ,  $\text{PO}_4^{3-}$ , and  
 187  $\text{O}_2$ , respectively. See Text S2 for more details and figures S1 and S2 for a comparison  
 188 to Peters, Jenkins, et al. (2018)'s cited parameter weights.

189 We also assessed the sensitivity of the OMP method to our chosen parameter weights  
 190 using a monte carlo routine. The default weights were perturbed by up to 20% using a  
 191 random number generator, 'RandomState' in python's numpy package, using fixed seed  
 192 '1234.' The analysis was re-run with each set of perturbed parameter weightings ( $n=20$ ).  
 193 We then calculated the standard deviation of residuals resulting from the sets of perturbed  
 194 parameter weighting. A low standard deviation in residuals indicates low sensitivity of  
 195 results to parameter weighting.

### 196 **2.2.3 Nutrient regeneration and assimilation**

197 When fitting water mass fractions to observations from GP15, the concentrations  
 198 of phosphate, oxygen, and nitrate (but not silicate) were allowed to be affected by pro-  
 199 duction and remineralization of organic matter. A fixed ratio of -9.68:1 was used to re-  
 200 late the consumption of oxygen to the regeneration of nitrate (Broecker, 1974; Peters,  
 201 Jenkins, et al., 2018), while a flexible regeneration ratio was used for oxygen to phos-  
 202 phate (O:P; range -96.5:1 to -305.6:1) to account for variable carbon to phosphate (C:P)  
 203 ratios observed throughout the Pacific. This range in O:P was derived by assuming a  
 204 C : N : O ratio of 106:16:-155 (Anderson, 1995; Peters, Jenkins, et al., 2018), and vary-  
 205 ing the amount of P relative to everything else to match the upper and lower limits for  
 206 C:P in the Pacific Ocean (which were 66:1 and 209:1) (Teng et al., 2014). For example,  
 207 a C:P ratio of 66:1, combined with an O:C ratio of -155:106 yields an O:P ratio of -96.5:1.  
 208 The solver in the OMP code finds the best fit to the observations, varying the water mass  
 209 fractions and the amount of oxygen consumed or nutrients regenerated, and the ratio  
 210 between changes in  $\text{O}_2$  and changes in P needed to fit the observations (Shrikumar et  
 211 al., 2022).

### 212 **2.2.4 Thermocline water mass analysis**

213 The potential density anomaly ( $\sigma_0$ ) surfaces that defined our thermocline bound-  
 214 aries varied from station to station, based on the  $\sigma_0$  gradient of GP15 CTD data for each  
 215 station (Text S3) (Cutter et al., 2020). The upper thermocline boundary was set where  
 216 either 25% of the maximum  $\sigma_0$  gradient ( $\frac{\partial\sigma_0}{\partial z}$ ) was found or where  $\frac{\partial\sigma_0}{\partial z}$  reached  $0.01 \text{ kg/m}^4$ ,

**Table 1.** Thermocline water mass definitions and penalties used in the thermocline OMP analysis. The potential density anomaly ( $\sigma_0$ ) range is the  $\sigma_0$  range of endmembers for each  $0.01 \text{ kg m}^{-3}$  increment of  $\sigma_0$  available and extracted. The lowest  $\sigma_0$  of the range is the lowest  $\sigma_0$  at which we were able to obtain an endmember based on GLODAP v2 data for a water mass definition region (Olsen et al., 2016; Key et al., 2015; Lauvset et al., 2021). Endmembers were only extracted for  $\sigma_0 \leq 27.00 \text{ kg m}^{-3}$ .

water mass	latitude range	longitude range	$\sigma_0$ ( $\text{kg m}^{-3}$ ) range	latitude penalty	sources
SPSTSW	15°S-20°S	142°W-152°W	22.40-27.00	north of equator	Fiedler and Talley (2006)
SPCW	20°S-30°S	130°W-152°W	22.79-27.00	north of 5°N	Sprintall and Tomczak (1993)
ESSW	5°S-5°N	80°W-90°W	19.56-27.00	north of 20°N	Wyrski (1967); Peters, Jenkins, et al. (2018)
ENPCW	16°N-26°N	170°W-140°W	21.91-27.00	south of equator	Seckel (1968); Talley (2011); Tomczak and Godfrey (2003a)
PSUW	50°N-58°N	155°W-140°W	23.71-27.00	south of 20°N	Thomson and Krassovski (2010)

**Table 2.** Intermediate and deep water mass definitions, number of subtypes (also referred to as archetypes), and penalties used in the intermediate and deep water OMP analysis. The samples falling within the latitude, longitude, and potential density ( $\sigma_0$ ) definitions of each water mass were extracted from GLODAP v2 database (Olsen et al., 2016; Key et al., 2015; Lauvset et al., 2021). An archetype analysis was then conducted to obtain water mass endmembers for the number of subtype(s) specified for a water mass.

water mass	latitude range	longitude range	$\sigma_0$ ( $\text{kg m}^{-3}$ )	no. of subtypes	latitude penalty	$\sigma_0$ penalty	sources
SPCW	20°S-30°S	130°W-152°W	25.29-26.86	2	north of 5°N	$\geq 27.4$	Sprintall and Tomczak (1993)
ESSW	5°S-5°N	80°W-90°W	25.29-26.86	2	north of 20°N	$\geq 27.2$	Wyrčki (1967); Peters, Jenkins, et al. (2018)
ENPCW	16°N-26°N	170°W-140°W	25.29-26.5	2	south of equator	$\geq 27$	Seckel (1968); Talley (2011); Tomczak and Godfrey (2003a)
PSUW	50°N-58°N	155°W-140°W	25.29-26.5	2	south of 20°N	$\geq 27.5$	Thomson and Krassovski (2010)
AAIW	55°S-43°S	90°W-80°W	27.05-27.15	2	north of 10°N	$\geq 27.6$	Iudicone et al. (2007); Talley (2011); Schmitz Jr (1996)
EqIW	5°S-5°N	80°W-90°W	26.86-27.3	2	north of 20°N	$\geq 27.2$	Wyrčki (1967); Peters, Jenkins, et al. (2018); Bostock et al. (2010); Reid (1965)
NPIW	36.5°N-39°N	148°E-154°E	26.4-26.9	3	north of 10°N	none	Yasuda (1997)
UCDW	44.5°S-49.5°S	157°W-147°W	27.35-27.75	1	north of 10°N	$\leq 27.3$	Peters, Jenkins, et al. (2018); Talley (2011); Orsi et al. (1995)
LCDW	61.5°S-66.5°S	150°E-100°W	27.79-27.83	2	north of 40°N	$\leq 27.7$	Peters, Jenkins, et al. (2018); Orsi et al. (1999)
AABW	61.5°S-66.5°S	150°E-100°W	$\geq \sigma_4$ of 46.04	1	north of 30°N	$\geq 27.6$	Peters, Jenkins, et al. (2018); Orsi et al. (1999)
PDW	39°N-51°N	170°W-133°W	27.2 to $\sigma_4$ of 45.88	3	none	none	Kawabe and Fujio (2010); Haley et al. (2014); Talley (2011)

217 whichever was shallower. The lower bound of the thermocline was set where  $\frac{\partial\sigma_0}{\partial z}$  returned  
 218 to  $0.003 \text{ kg/m}^4$ . These boundaries can be seen in  $\sigma_0$  and depth space in Figure S3 and  
 219 resulted in 341 GP15 samples being included in the GP15 analysis.

220 In order to define the thermocline endmember properties, data were extracted from  
 221 Global Ocean Data Analysis Project version 2 (GLODAPv2) (Olsen et al., 2016; Key  
 222 et al., 2015; Lauvset et al., 2021) within the latitude, longitude, and  $\sigma_0$  ranges for each  
 223 thermocline water mass, described below. A cubic spline was fit to the density profile  
 224 of each parameter for each water mass and used to obtain an endmember for every  $0.01$   
 225  $\text{kg m}^{-3}$  increment of  $\sigma_0$  (Text S4). A separate water mass analysis was then conducted  
 226 for each  $0.01 \text{ kg m}^{-3}$  increment of  $\sigma_0$  within each station’s individual thermocline bound-  
 227 aries. Waters above the thermocline were not included in the analysis due to seasonal  
 228 and/or annual variations in temperature, salinity, and nutrients (Fiedler & Talley, 2006;  
 229 Musgrave et al., 1992; Ueno & Yasuda, 2000). However, a qualitative characterization  
 230 of these surface waters is given in relation to the hydrography and nutrient distributions.

231 The water masses included in the thermocline OMP analysis are as follows: South  
 232 Pacific Subtropical Surface Water (SPSTSW), South Pacific Central Water (SPCW), Equa-  
 233 torial Subsurface Water (ESSW), Eastern North Pacific Central Water (ENPCW), and  
 234 Pacific Subarctic Upper Water (PSUW). Each of these water masses has a defined lat-  
 235 itude and longitude range chosen to reflect where the waters are subducted, with prefer-  
 236 ence given to proximity to the transect when subduction occurs over a large area (Ta-  
 237 ble 1 and Figure 1).

238 SPSTSW is formed in the South Pacific Subtropical Gyre where evaporation ex-  
 239 ceeds precipitation, resulting in some of the saltiest waters found in the Pacific (Fiedler  
 240 & Talley, 2006). Although it does influence the upper thermocline of the GP15 transect,  
 241 it is considered a surface water mass. The geographic range we used to define this wa-  
 242 ter mass was defined proximally, due to the variability in surface water salinity, and ac-  
 243 cording to circulation patterns. Anything west of GP15 ( $152^\circ\text{W}$ ) was not included in the  
 244 definition range given the westward flow of the South Equatorial Current (Talley, 2011).

245 SPCW is formed when surface waters between  $155^\circ\text{E}$  to  $130^\circ\text{W}$  in the south Pa-  
 246 cific subtropical gyre are subducted (Sprintall & Tomczak, 1993). This water mass can  
 247 be found around a  $\sigma_0$  of  $26.5 \text{ kg m}^{-3}$  between  $10^\circ\text{S}$  and the Subantarctic Front, around  
 248  $55^\circ\text{S}$  (Talley, 2011). Compared to ENPCW (salinity around 35 at its shallowest reaches),  
 249 SPCW is more saline (salinity around 36 at its shallowest reaches) (Emery & Meincke,  
 250 1986). The geographic range used for its origin in the literature was modified to align  
 251 with the subtropical gyre’s circulation (Sprintall & Tomczak, 1993; Peters, Jenkins, et  
 252 al., 2018). Again, anything west of our transect ( $152^\circ\text{W}$ ) was not included in the def-  
 253 inition range given the westward flow of the South Equatorial Current (Talley, 2011).

254 ESSW originates from the the west Pacific and is transported via the Equatorial  
 255 Countercurrents and Undercurrents that upwell in the eastern tropical Pacific to form  
 256 ESSW (Montes et al., 2014; Stramma et al., 2010). Its core is fairly shallow around  $\sigma_0$   
 257 of 24 to  $25 \text{ kg m}^{-3}$  (Fiedler & Talley, 2006; Silva et al., 2009). Most strongly present be-  
 258 tween  $10^\circ\text{N}$  and  $10^\circ\text{S}$ , ESSW is characterized by high temperature ( $7.0\text{-}23.0^\circ\text{C}$ ) and salin-  
 259 ity ( $34.5\text{-}36.0$ ) (Emery & Meincke, 1986; Silva et al., 2009; Wyrтки, 1967). Its salinity  
 260 maximum coincides with a dissolved oxygen minimum and high nitrate and phosphate  
 261 concentrations (Silva et al., 2009). The geographic range used to define ESSW in this  
 262 analysis was chosen to reflect the area where the water is upwelled off the coast of South  
 263 America before flowing westward along the equator as ESSW (Peters, Jenkins, et al., 2018;  
 264 Wyrтки, 1967).

265 ENPCW is formed via surface water subduction in the north Pacific subtropical  
 266 gyre between  $26^\circ\text{N}$  and  $16^\circ\text{N}$ , and its core occupies  $\sigma_0$  of  $25\text{-}25.8 \text{ kg m}^{-3}$  (Seckel, 1968;  
 267 Bograd et al., 2019). ENPCW is found east of  $170^\circ\text{W}$  and between the North Equato-

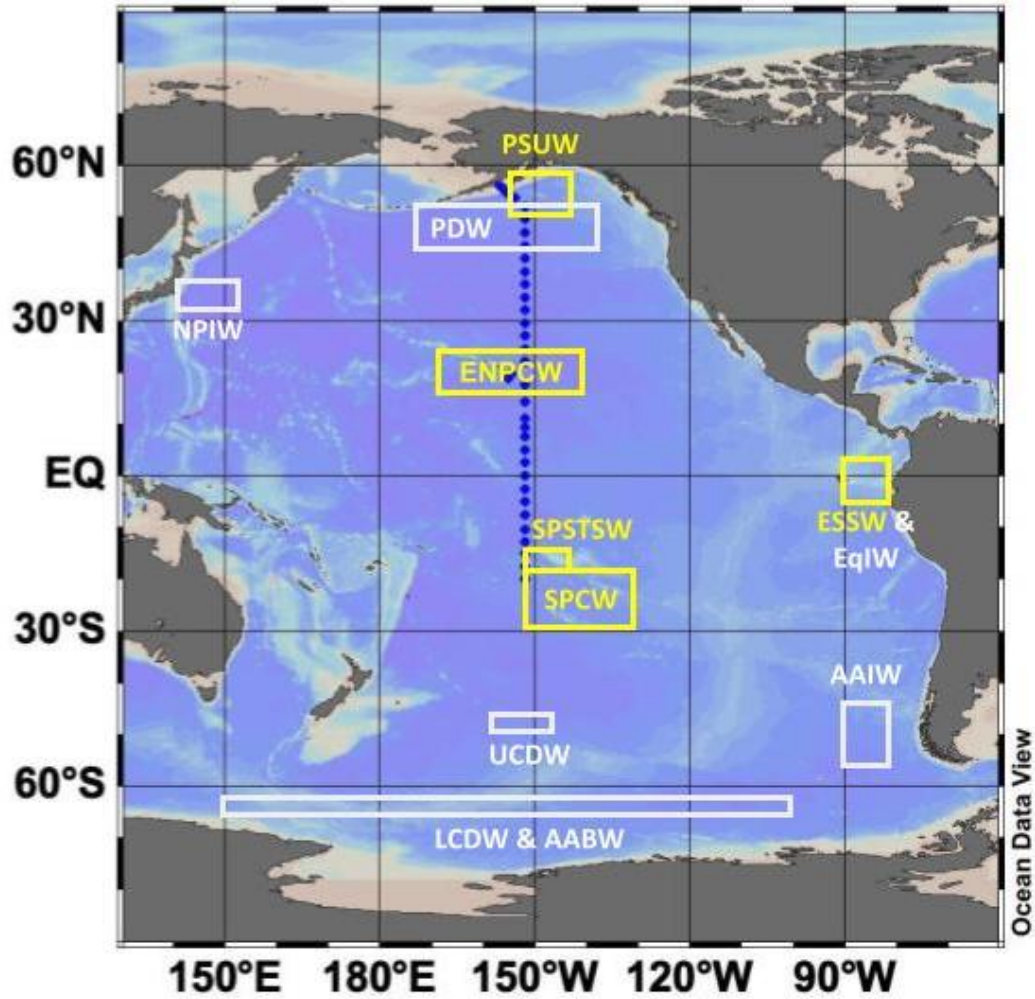


**Figure 1.** The latitude and longitude definition ranges for the thermocline water masses are in yellow. The ranges for the intermediate and deep waters are in white. The water mass names can be found in the 'Acronyms' section at the end of the paper.

268 rial Countercurrent (located 3-10°N) and 40°N (Tomczak & Godfrey, 2003b). The lat-  
 269 itudinal range used for this analysis was defined as 16°N-26°N (Seckel, 1968). The bound-  
 270 ary between the Eastern and Western North Pacific Central Waters according to Tomczak  
 271 and Liefvink (2005) is 170°W. This serves as the western boundary of the ENPCW for  
 272 our analysis while 140°W, the longitude of the California Current System, is the east-  
 273 ern boundary (Talley, 2011).

274 Cold subpolar surface waters are subducted around 50°N to form PSUW (Talley,  
 275 Sverdrup et al., 1942). PSUW is typically carried east along the Subarctic Front  
 276 until it hits the west coast of North America, moving south and mixing with central wa-  
 277 ter (Tomczak & Godfrey, 2003b; Sverdrup et al., 1942). Its core is found between a  $\sigma_0$   
 278 of 25.4 and 25.6  $\text{kg m}^{-3}$  (Bograd et al., 2019). PSUW is characterized by relatively high  
 279 oxygen (250-300  $\mu\text{mol m}^{-1}$ ), low temperature (3.0-15.0°C), and low salinity (32.6-33.6%)  
 280 compared to the other thermocline water masses on this transect (Bograd et al., 2019;  
 281 Cepeda-Morales et al., 2013; Emery & Meincke, 1986; Yuan & Talley, 1992; Tomczak &  
 282 Liefvink, 2005; Schroeder et al., 2019). Large fractions of PSUW are not expected south  
 283 of the Subarctic Frontal Zone, which is at approximately 42°N (Talley, 2011). The ge-  
 284 ographic range used to define PSUW in this analysis was based off the area of PSUW  
 285 shown in Thomson and Krassovski (2010). Due to the variability within the Gulf of Alaska,  
 286 and therefore PSUW water properties, 155°W to 140°W were chosen as the longitudi-  
 287 nal range for this water mass (Musgrave et al., 1992).

### 288 *2.2.5 Deep and intermediate water mass analysis*

289 The water masses in the intermediate and deep water OMP analysis (682 samples)  
 290 include Antarctic Intermediate Water (AAIW), Equatorial Intermediate Water (EqIW),  
 291 North Pacific Intermediate Water (NPIW), Upper Circumpolar Deep Water (UCDW),  
 292 Lower Circumpolar Deep Water (LCDW), Antarctic Bottom Water (AABW), and Pa-  
 293 cific Deep Water (PDW) (Figure 1). Thermocline water masses PSUW, ENPCW, ESSW,  
 294 and SPCW were also included in the intermediate and deep water OMP analysis to ac-  
 295 count for any mixing between the lower thermocline and intermediate waters. A latitude,  
 296 longitude, and density range was chosen for each water mass based on its origin, or lit-  
 297 erature description of where the water mass is subducted, or its water type is defined  
 298 (Table 2). The GLODAP v2 data were then extracted for these ranges (Olsen et al., 2016;  
 299 Key et al., 2015; Lauvset et al., 2021). The endmember properties for each water mass,  
 300 were derived from the extracted GLODAPv2 data using an archetype analysis, with some  
 301 water masses including multiple subtypes (archetypes) (Table S1) (Cutler & Breiman,  
 302 1994).

303 An archetype analysis is used to identify the points across a multidimensional dataset  
 304 that can be used to define a convex shape around the observations. In other words, the  
 305 archetype analysis finds the best endmembers across the water properties of the data that,  
 306 if plotted over all the water properties at once, would "encompass" the most observa-  
 307 tions. The number of archetypes used here depended on the number of archetypes needed  
 308 to best describe the water mass data, with support from the literature. See Shrikumar  
 309 et al. (2022) for more information on archetype analysis used to determine water mass  
 310 subtypes for the OMP water mass analysis.

311 The latitude and longitude ranges defining thermocline water masses PSUW, EN-  
 312 PCW, ESSW, and SPCW were discussed in Section 2.2.4. The  $\sigma_0$  ranges for these ther-  
 313 mocline water masses used in the intermediate and deep water analysis were determined  
 314 by the range in the bottom boundary of the thermocline across the section (25.29 to 26.86  
 315  $\text{kg m}^{-3}$ ; Figure S3b). This was done to capture characteristics of the bottom of the ther-  
 316 mocline, the water most likely to mix with intermediate waters. While the full  $\sigma_0$  range  
 317 was used for ESSW and SPCW, the range was reduced to 25.29 to 26.5  $\text{kg m}^{-3}$  for PSUW

318 and ENPCW to minimize overlap with the definition of NPIW ( $\sigma_0$  from 26.4 - 26.9 kg  
319  $\text{m}^{-3}$ ).

320 NPIW and Pacific AAIW can both be identified by salinity minima (salinities around  
321 34) in their respective hemispheres. The NPIW is formed and influenced by the north-  
322 west Pacific subtropical gyre, Okhotsk Sea, and Alaskan Gyre (Ueno & Yasuda, 2003;  
323 You et al., 2000; Talley et al., 1991, 1995; Yasuda, 1997; Van Scoy et al., 1991). NPIW  
324 increases in salinity and decreases in oxygen along its advective path across the north  
325 Pacific (Talley, 1993). We chose an origin range from the northwest source waters (34°N  
326 to 37°N and 140°E to 153°E) (Yasuda, 1997). The  $\sigma_0$  range chosen (26.5 to 27.4  $\text{kg m}^{-3}$ )  
327 encompasses the salinity minimum typically found at a  $\sigma_0$  of 26.9  $\text{kg m}^{-3}$  (You et al.,  
328 2003). NPIW is mostly confined to the North Pacific Subtropical Gyre, south of 46°N  
329 (Talley et al., 1991; Talley, 1993).

330 Unlike NPIW being confined to the subtropical gyre, AAIW is present through-  
331 out the subtropical South Pacific and tropical Pacific south of 15°N-10°N (Talley, 2011,  
332 1993). The source waters for AAIW are from the Southwest Pacific (Talley, 2011; Hartin  
333 et al., 2011; Molinelli, 1981; Piola & Georgi, 1982; Georgi, 1979; McCartney, 1977; Sloyan  
334 & Rintoul, 2001). AAIW is identified by its characteristic local salinity minimum and  
335 oxygen maximum. The salinity minimum of AAIW can be found in the  $\sigma_0$  range of 27.05  
336 to 27.15  $\text{kg m}^{-3}$  (Talley, 2011). The latitude and longitude ranges used were 43-55°S and  
337 80-90°W, respectively (Iudicone et al., 2007; Peters, Jenkins, et al., 2018).

338 Compared to AAIW, EqIW has lower oxygen and higher nutrients, temperature,  
339 and salinity (Peters, Jenkins, et al., 2018; Bostock et al., 2010, 2013). EqIW is formed  
340 in the eastern equatorial Pacific and found primarily between 15°S and 15°N (Bingham  
341 & Lukas, 1995; Wyrтки, 1967; Bostock et al., 2010). Some authors have separated EqIW  
342 into northern and southern subtypes (Bingham & Lukas, 1995; Bostock et al., 2010). The  
343 northern subtype has a double salinity minimum, while the southern subtype can be found  
344 on two  $\sigma_0$  surfaces, has a single salinity minimum, and has low oxygen (Bingham & Lukas,  
345 1995). We used a range of latitude and longitude (5°S - 5°N) that should include both  
346 subtypes and allowed the archetype analysis to define two endmembers for EqIW. While  
347 the latitude and longitude ranges used in the analysis for EqIW align with that of the  
348 thermocline water mass ESSW (Peters, Jenkins, et al., 2018; Wyrтки, 1967), the  $\sigma_0$  range  
349 for EqIW (26.86 - 27.3  $\text{kg m}^{-3}$  (Reid, 1997; Bostock et al., 2010)) places it below the  
350 thermocline.

351 Upper Circumpolar Deep Water (UCDW) is formed from modified PDW and moves  
352 southward on an isopycnal surface similar to PDW until it is upwelled in the Southern  
353 Ocean, south of the Antarctic Circumpolar Current (ACC) (Faure & Speer, 2012; Orsi  
354 et al., 1995). UCDW coincides with a local nutrient maximum and oxygen minimum (Whitworth III  
355 et al., 1985; Talley, 2013; Orsi et al., 1995). UCDW can be found between the Hawai-  
356 ian Islands (19.89°N where PDW mixes with UCDW) and the ACC (Talley, 2011; Kawabe  
357 & Fujio, 2010). As mentioned previously in Peters, Jenkins, et al. (2018), the proper-  
358 ties of UCDW change during transport, and it is best defined relatively far from PDW  
359 to avoid overlap between the endmember properties of UCDW and PDW (Kim et al.,  
360 2013). The origin latitude and longitude ranges used here were 45.5-49.5°S and 147-157°W,  
361 respectively (Peters, Jenkins, et al., 2018). UCDW's  $\sigma_0$  ranges from 27.35 - 27.75  $\text{kg m}^{-3}$   
362 near the northern edge of the ACC, close to the chosen latitudinal and longitudinal ranges  
363 (Orsi et al., 1995).

364 PDW is formed via internal mixing and upwelling of water masses and is present  
365 throughout the Pacific Ocean (Talley, 2011). PDW flows southward primarily along the  
366 eastern boundary (Reid, 1997), carrying its low oxygen, high silicate signals. Our anal-  
367 ysis used three subtypes, in keeping with classic definitions Talley (2011), defined within  
368 the ranges 39°N-51°N and 170°W-133°W (Kawabe & Fujio, 2010).

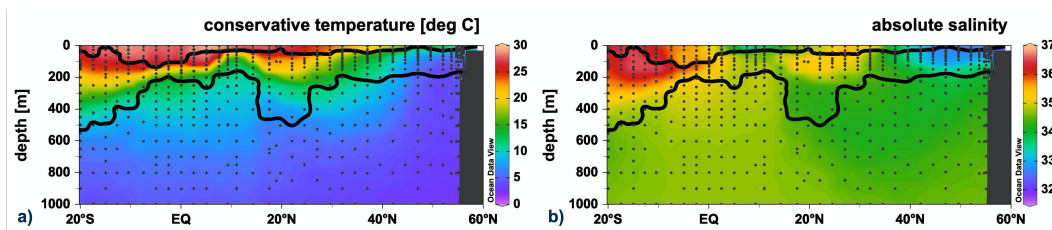


**Figure 2.** The panels, a) conservative temperature ( $^{\circ}\text{C}$ ) and b) absolute salinity, include the upper 1000 m along GP15. The black contour lines represent the upper and lower thermocline boundaries.

369 LCDW is identified by the vertical salinity maximum in the Antarctic Circumpolar  
 370 Current (ACC) (Talley, 2011). This high salinity originates from NADW, as it en-  
 371 ters into the ACC via the southwestern Atlantic Ocean, mixes with the circumpolar deep  
 372 water, and enters the Pacific Ocean (Whitworth III et al., 1985; Orsi et al., 1995). LCDW  
 373 erodes and mixes into PDW from south to north (Talley, 2011). LCDW was defined here  
 374 at a latitude between  $61.5^{\circ}\text{S}$  -  $66.5^{\circ}\text{S}$ , similar to earlier studies (Peters, Jenkins, et al., 2018),  
 375 and longitudes between  $150^{\circ}\text{E}$  -  $160^{\circ}\text{W}$ , about width of the Pacific Ocean.

376 AABW is formed by deep convection at the Antarctic continental margin and does  
 377 not extend much beyond  $30^{\circ}\text{N}$  in the Pacific Ocean (Orsi et al., 1999; Lee et al., 2019).  
 378 AABW is found within the ACC below the circumpolar deep water. The latitude range  
 379 chosen,  $61.5^{\circ}\text{S}$  to  $66.5^{\circ}\text{S}$ , was similar to prior studies (Peters, Jenkins, et al., 2018). The  
 380 longitude range is about the width of the Pacific Ocean ( $150^{\circ}\text{E}$  to  $160^{\circ}\text{W}$ ) as AABW is  
 381 found throughout the South Pacific. The  $\sigma_0$  referenced to 4000 db ( $\sigma_4$ ) for this water  
 382 mass was taken as greater than  $46.04 \text{ kg m}^{-3}$  (Orsi et al., 1999).

### 383 3 Results

#### 384 3.1 Temperature and salinity

385 The temperature and salinity distributions for GP15 reflect surface conditions, cur-  
 386 rents, and key water masses along the transect (Figure 2). In the upper 400 m between  
 387  $20^{\circ}\text{S}$  and the equator, evaporation exceeds precipitation yielding the warmest, saltiest  
 388 waters of the transect (Talley, 2011). These waters primarily correspond to South Pa-  
 389 cific Subtropical Surface Water (SPSTSW), transitioning to slightly less saline South Pa-  
 390 cific Central Water (SPCW) through lateral and vertical mixing (Fiedler & Talley, 2006).  
 391 Below the thermocline in the southern hemisphere, a salinity minimum is observed around  
 392 750 m, most strongly at  $20^{\circ}\text{S}$  (Figure 2b). This is indicative of Antarctic Intermediate  
 393 Water (AAIW) (Talley, 2011; Fiedler & Talley, 2006). We also see relatively low salin-  
 394 ity at the surface around  $10^{\circ}\text{N}$ . This is likely due to high precipitation in the Intertrop-  
 395 ical Convergence Zone (ITCZ) (Marshall et al., 2014). Underneath these low-salinity sur-  
 396 face waters is a shoaling of cooler water, the equatorial subsurface water (Fiedler & Tal-  
 397 ley, 2006; Wyrтки, 1967).

398 North of  $17.5^{\circ}\text{N}$ , there is an abrupt increase in surface salinity. This marks the North  
 399 Equatorial Current, separating equatorial waters from the Eastern North Pacific Central  
 400 Water (ENPCW) in the North Pacific Subtropical Gyre (Talley, 2011). Salinity is  
 401 higher at the surface around  $25^{\circ}\text{N}$  than in the ITCZ but lower than the southern part  
 402 of the transect (Seckel, 1968; Tomczak & Godfrey, 2003a). This is likely due to higher  
 403 rates of net evaporation in the South Pacific Subtropical Gyre compared to the North  
 404 Pacific Subtropical Gyre (Talley, 2011). Below the ENPCW, between 200-800 m, is a  
 405 salinity minimum that marks North Pacific Intermediate Water (NPIW) (Fiedler & Tal-

406 ley, 2006). Further north along the section, the North Pacific Current separates the Sub-  
 407 arctic Frontal Zone and Subtropical Frontal Zone and is indicated by a large salinity gra-  
 408 dient in the upper 200 m between 30-40°N (Figure 2b).

409 North of 40°N, decreasing temperature and salinity in the upper 200 m mark the  
 410 presence of the Subarctic Front. Pacific Subarctic Upper Water (PSUW) is indicated by  
 411 fresh, cold water seen at the surface between 40°N and the northern end of the transect  
 412 (Tomczak & Godfrey, 2003a). Precipitation exceeds evaporation in the Alaskan Gyre (Royer,  
 413 1979). Coastal mountain ranges bordering the Alaskan Gyre increase the precipitation  
 414 effect, and freshwater from regional glaciers, rivers, and run-off further freshen surface  
 415 waters (Royer, 1979; Brown et al., 2010). We see this distinctly in the upper 50 m in the  
 416 most northern part of our transect, which is evidence of the Alaskan stream (Musgrave  
 417 et al., 1992).

### 418 3.2 Oxygen and nutrients

419 Dissolved oxygen [ $O_2$ ] concentrations reflect the distributions of ventilated mode  
 420 waters, low oxygen shadow zones (location of the oldest Pacific waters), and respiration  
 421 during subsurface transit since a water mass last surfaced (Holzer et al., 2021). At 20°S  
 422 around 550 m, relatively high  $O_2$  (slightly higher than  $200 \mu\text{mol kg}^{-1}$ ) is likely Sub-Antarctic  
 423 Mode Water (SAMW) (Rafter et al., 2013) (Figure 3a). Underneath is a local oxygen  
 424 minimum around 1500 m from Upper Circumpolar Deep Water (UCDW) (Figure S4c)  
 425 (Tomczak & Liefink, 2005). Lower Circumpolar Deep Water (LCDW) at 20°S around  
 426 3500 m and especially Antarctic Bottom Water (AABW) around 15°S below 4000 m have  
 427 higher oxygen than UCDW (Figure S4c) (Orsi et al., 1995, 1999). At 5°S and 10°N, low  
 428 oxygen in the upper 200-600m are likely signals from the Peruvian oxygen deficient zone  
 429 (ODZ) and Eastern Tropical North Pacific ODZ (Figure 3a). The signal is stronger in  
 430 the north than the south likely due to the transect's closer proximity to the Eastern Trop-  
 431 ical North Pacific ODZ. For many stations north of the equator, an oxygen deficit around  
 432 1000 m corresponds with high nitrate (Figure 3c) and phosphate (Figure 3d) concentra-  
 433 tions (see Figure S4 for full depth profiles). This is a signal of PDW's accumulation of  
 434 regenerated nutrients (Östlund & Stuiver, 1980; Hautala & Hammond, 2020). Around  
 435 35°N between 200 m and 400 m,  $O_2$  is relatively high (between 200 and  $250 \mu\text{mol kg}^{-1}$ ).  
 436 This is likely North Pacific Central Mode Water (NPCMW) (Mecking & Warner, 2001).  
 437 North of 40°N, [ $O_2$ ] is relatively high ( $260$  to  $307.78 \mu\text{mol kg}^{-1}$ ) in the upper 150 m (Fig-  
 438 ure 3a). This oxygen feature coincides with a temperature minimum ( $4.54$  to  $14.75^\circ\text{C}$ )  
 439 characteristic of Dichothermal Water (DtW) (Talley, 2011; Haley et al., 2014).

440 Nitrate, phosphate, and silicate concentrations were all low in the upper 250 m of  
 441 the subtropical gyres, reaching undetectable levels for all nutrients in the upper 100 m  
 442 (Figure 3b,c,d). This matches literature expectation as the subtropical gyres are oligo-  
 443 trophic (Talley, 2011). Nitrate and phosphate maxima extend southward around 1500  
 444 m in UCDW (Figure S4e,f) (Tomczak & Liefink, 2005). Relatively low phosphate and  
 445 nitrate concentrations in the deepest waters in the southern part of our transect (around  
 446 3500 m at 20°S and below 4000 m between 15°S and the equator) are consistent with the  
 447 presence of LCDW and AABW there (Figure S4e,f) (Orsi et al., 1995, 1999). High sil-  
 448 icate waters were seen in the northern part of the transect, with a double silicate max-  
 449 imum between 2000-2500 m and 4000-5000 m around 40°N (Figure S4d) (Edmond et al.,  
 450 1979; Talley & Joyce, 1992). The mid depth maximum is thought to originate from the  
 451 western Pacific, while the near-bottom maximum derives from benthic fluxes in the east-  
 452 ern north Pacific basin (Hou et al., 2019; Hautala & Hammond, 2020).

453 The concentrations of nitrate and phosphate can be used to derive the distribu-  
 454 tion of  $N^*$ :

$$N^* = N - 16 * P + 2.9 \mu\text{mol/kg}^3 \quad (1)$$

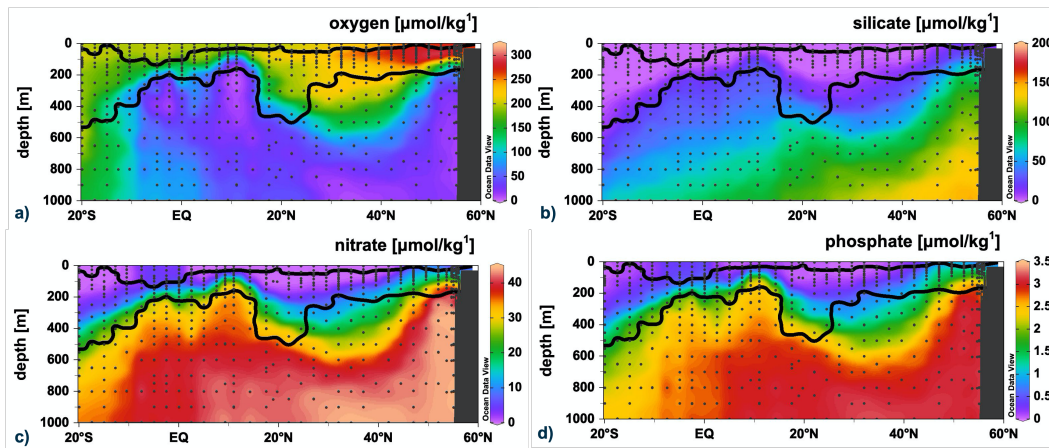


**Figure 3.** The panels, a) dissolved oxygen concentrations ( $\mu\text{mol kg}^{-1}$ ), b) silicate concentrations ( $\mu\text{mol kg}^{-1}$ ), c) nitrate concentrations ( $\mu\text{mol kg}^{-1}$ ), and d) phosphate concentrations ( $\mu\text{mol kg}^{-1}$ ), include the upper 1000 m of GP15. The black contour lines represent the upper and lower thermocline boundaries.

455 which is a measure of nitrate deficit or excess relative to phosphate (Deutsch et al., 2001).  
 456 This quantity gives insights into whether nitrogen gain (via  $\text{N}_2$  fixation) or loss (via den-  
 457 trification) has occurred in a water parcel (Gruber & Sarmiento, 1997). Generally, a pos-  
 458 itive  $\text{N}^*$  indicates the influence of  $\text{N}_2$  fixation while a negative  $\text{N}^*$  indicates the effects  
 459 of denitrification. At  $5^\circ\text{S}$  and  $10^\circ\text{N}$ , low  $\text{N}^*$  in the upper 200-600 m, coincides with low  
 460 oxygen areas previously suggested to derive from the the Eastern Tropical South Pacific  
 461 and Eastern Tropical North Pacific ODZs, respectively (Sarmiento, 2013). In the North  
 462 Pacific Subtropical Gyre, we see low  $\text{N}^*$  values (around -4) near 1000 m corresponding  
 463 with the nitracline and PDW's oldest waters (Figure 4; see Figure S5 for the full water  
 464 column).  $\text{N}_2$  fixation and denitrification are typically spatially separated, with  $\text{N}_2$  fix-  
 465 ation occurring largely in surface waters and denitrification occurring in low-oxygen ther-  
 466 mocline waters and shallow marine sediments. However, the lowest  $\text{N}^*$  values on GP15  
 467 were found in the upper 200 m around  $50^\circ\text{N}$  (Figure 4), coinciding with high oxygen (Fig-  
 468 ure 3a). This could be a sedimentary denitrification signal but is somewhat separated  
 469 from the shelf waters and may be imported from elsewhere (Lehmann et al., 2019). The  
 470 lowest  $\text{N}^*$  value flagged as "likely good" is  $-6.26 \mu\text{mol kg}^{-1}$  at  $47^\circ\text{N}$ , 41.3 dbar (Figure  
 471 S6).

### 472 3.3 Thermocline boundaries

473 The beginning of Section 2.2.4 describes how the thermocline boundaries are defined.  
 474 The upper boundary of the thermocline, which can also be called the mixed layer  
 475 depth, along GP15 occurred between  $20.83 \text{ kg m}^{-3}$  and  $24.63 \text{ kg m}^{-3}$  (5.40 m - 122.39  
 476 m) (Figure S3). The boundary between the thermocline and intermediate waters occurred  
 477 between  $25.29 \text{ kg m}^{-3}$  and  $26.86 \text{ kg m}^{-3}$  (85.20 m - 493.28 m). The lower boundary is  
 478 relatively shallow (around 225 m) near the equator, possibly due to equatorial upwelling  
 479 (Figure S3a). The  $\sigma_0$  range of the thermocline is relatively wide in the subtropical gyres  
 480 around  $20^\circ\text{S}$  and  $20^\circ\text{N}$ , likely due to Ekman pumping/downwelling influenced by the sub-  
 481 tropical gyres. The thermocline boundaries are narrower in the Alaskan Gyre than the  
 482 subtropical gyres, especially north of  $55^\circ\text{N}$  (Figure S3). The narrowing in the Alaskan  
 483 Gyre may be due to Ekman upwelling, and the especially narrow boundaries around  $55^\circ\text{N}$   
 484 are likely due to a shallower environment on the coastal shelf of Alaska.

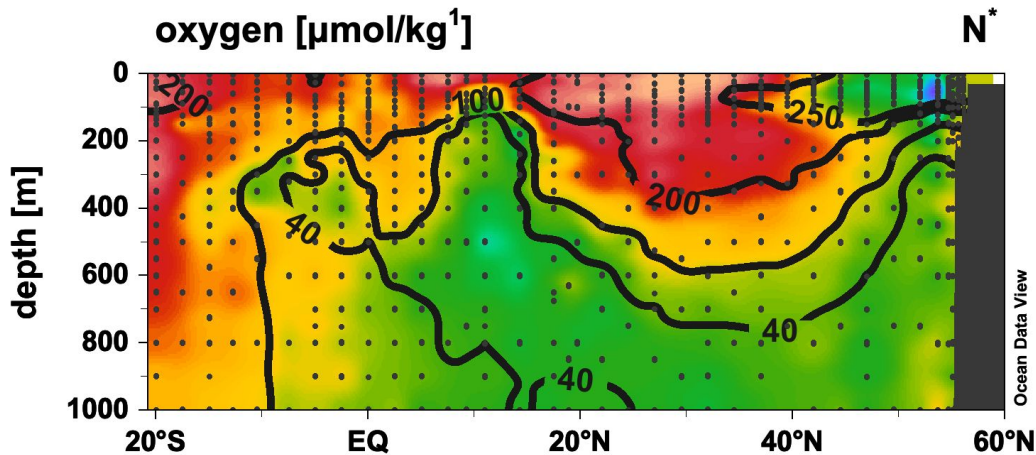


**Figure 4.**  $N^*$  ( $\mu\text{mol kg}^{-1}$ ) with dissolved oxygen ( $\mu\text{mol kg}^{-1}$ ) contours in the upper 1000 m along the GP15 transect.

485

### 3.4 Phosphate regeneration and assimilation ratios

486

487

488

489

490

491

492

493

494

495

The oxygen:phosphate (O:P) ratios used to represent organic matter remineralization (or production) were allowed to vary from  $-96.5:1$  to  $-305.6:1$ , which is derived from the range in the carbon to phosphate (C:P) ratios of organic matter observed throughout the Pacific Ocean ( $66:1$  to  $209:1$ ) (DeVries & Deutsch, 2014; Teng et al., 2014). We can look at both the amount of regenerated (or assimilated) phosphate that is inferred by the model, as well as the O:P ratio associated with it. However, when the amount of regenerated phosphate is very small, the derived O:P ratio is not very reliable. Therefore, we restrict our interpretation of the O:P ratio to samples where regenerated (or assimilated) phosphate is greater than  $0.25 \mu\text{mol kg}^{-1}$  ( $-0.25 \mu\text{mol kg}^{-1}$  for assimilation) (Figure S7).

496

497

498

499

500

501

502

503

The amount of assimilated phosphate was more than  $0.25 \mu\text{mol kg}^{-1}$  only within the upper 500 m at certain latitudes along the section (Figure S7a). This quantity is negative because primary production removes phosphate from the water column relative to what would be supplied by end-member mixing. At the same time, oxygen would be produced via photosynthesis. Therefore, it make sense that assimilation would show up predominantly in the upper water column, where photosynthesis takes place. The ratio of oxygen production to phosphate assimilation was relatively low ( $96.5-141.8 \mu\text{mol kg}^{-1}$ ), possibly due to oxygen losses to the atmosphere.

504

505

506

507

508

509

510

511

512

513

514

515

The amount of regenerated phosphate was above  $0.25 \mu\text{mol kg}^{-1}$  within the upper 1500 m throughout the section (Figure S7b). Relatively high O:P ratios for regenerated phosphate were observed in the north and south subtropical gyres, while lower ratios of O:P were observed near the equator ( $13^\circ\text{S}-25^\circ\text{N}$ ), except where the section intersects ODZ signals (Section 3.2). These observations are generally in keeping with expectations that the lowest O:P ratios (lowest C:P) would be observed in the equatorial region, and the highest oxygen consumption O:P ratio (highest C:P) in the oligotrophic gyres (Teng et al., 2014; DeVries & Deutsch, 2014). Many of the Alaskan Gyre O:P ratios shown in Figure S7b coincide with the oldest waters of the Pacific characterized by low oxygen and high phosphate. Thus, we may not have observed low O:P ratios in the Alaskan Gyre because of pre-existing regenerated phosphate in our northern endmember.

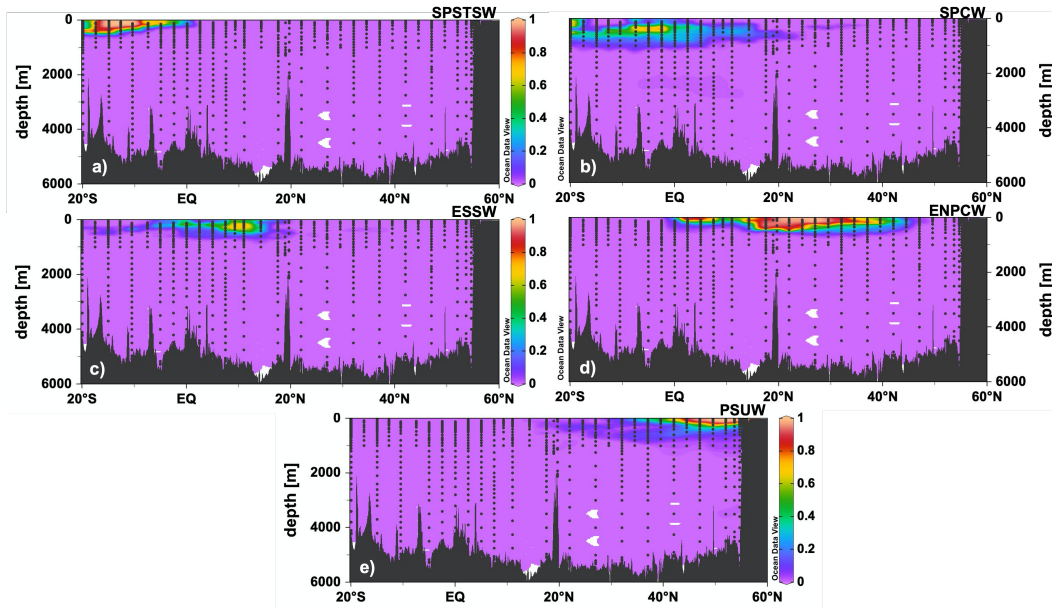


**Figure 5.** Thermocline water mass fractions for a) SPSTSW, b) SPCW, c) ESSW, d) ENPCW, and e) PSUW.

516

### 3.5 Distribution of Water Mass Fractions

517

518

519

520

521

522

523

524

525

526

527

528

529

530

531

532

533

534

535

536

537

The water mass fractions shown in figures 5 through 7 are from the OCIM-constrained OMP solution (Section 2.2.1) (Shrikumar et al., 2022). For water masses with subtypes, the individual water mass fractions for each subtype can be seen in Figure S8. SPSTSW dominated the upper thermocline between 10-15°S, and extended to the equator in lower amounts (Figure 5a) (Fiedler & Talley, 2006). Our results placed the maximum contribution of SPCW between 10°S and the equator (Figure 5b), although it extended further south to overlap its literature range (south of 10°S) (Talley, 2011). The Southern Equatorial Counter Current may have carried the relatively high fraction of SPCW to around 7°S on GP15. ESSW mixes into SPCW starting around the equator (Figure 5c). ESSW is observed between 5°N and 10°S (Emery & Meincke, 1986; Silva et al., 2009; Wyrki, 1967), although we see higher ESSW water mass fractions north of the equator due to the subtropical gyre boundary being closer to the equator in the south than the north (Fiedler & Talley, 2006; Talley, 2011). ESSW and ENPCW mix in the lower thermocline in the tropics, reaching a maximum contribution of ENPCW around 18°N (Figure 5d). ENPCW fills the thermocline between the North Equatorial Countercurrent (located 3-10°N) and 40°N, as expected from the literature (Tomczak & Godfrey, 2003b). ENPCW begins mixing with PSUW around 40°N (Figure 5e) (Tomczak & Godfrey, 2003b; Talley, 2011). As described in the literature, the thermocline in the northernmost part of GP15 is dominated by PSUW (Sverdrup et al., 1942). Our results also reflect some water mass mixing between thermocline and intermediate waters near the bottom of the thermocline.

538

539

540

541

542

543

544

The highest fractions of intermediate water masses, AAIW, PEqIW, and NPIW, were found just below the thermocline, between approximately 500 m and 1250 m (Figure 6). While AAIW is described in the literature and shown in our results as primarily in the southern hemisphere, it can extend as far north as the northern subtropical gyre at approximately 10°N-15°N (Talley, 2011, 1993). Our results show low fractions of AAIW extending as far north as 20°N, aligning with its salinity minimum around 750 m depth. The highest EqIW water mass fractions were found between the equator and

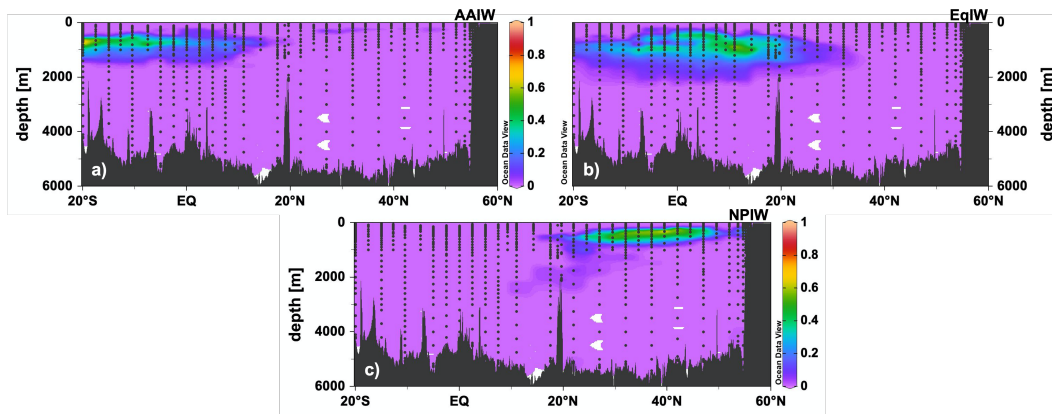


**Figure 6.** Intermediate water mass fractions for a) AAIW b) EqIW, and c) NPIW.

545 12.5°N. This falls within the literature range of between 15°S and 15°N (Reid, 1997; Silva  
 546 et al., 2009; Bostock et al., 2010; Reid, 1965). The equatorial water contributing to a greater  
 547 extent north of the equator may not be intuitive, but Fiedler and Talley (2006)’s place-  
 548 ment of AAIW and NPIW leave room for EqIW just north of the equator. NPIW was  
 549 mostly confined to the North Pacific Subtropical Gyre, south of 46°N, following the salin-  
 550 ity minimum as described in the literature (Talley et al., 1991; Talley, 1993). NPIW also  
 551 extended into the Alaskan Gyre, which is to be expected as the Alaskan Gyre is known  
 552 to play a role in NPIW formation (You et al., 2000).

553 Our results confirm the presence of UCDW, LCDW, and AABW in the deep wa-  
 554 ters of the southern hemisphere. UCDW dominated depths immediately below AAIW  
 555 (1000-2000 m), while LCDW was found below 2000 m (Figure 7). Upper Circumpolar  
 556 Deep Water (UCDW) is found where local nutrient maxima and oxygen minima over-  
 557 lap as shown in Figure S9 (Whitworth III et al., 1985; Talley, 2013; Orsi et al., 1995).  
 558 Lower Circumpolar Deep Water (LCDW) is primarily within the same densities as seen  
 559 in Talley (2011) (Figure S10). Only small water mass fractions of AABW were present,  
 560 and they were primarily confined to the deepest, southernmost part of the transect. This  
 561 aligns with the literature suggesting AABW does not extend much beyond 30°N in the  
 562 Pacific Ocean (Orsi et al., 1999; Lee et al., 2019). PDW dominates the deep water (ap-  
 563 proximately 1000 m and below) in the northern hemisphere, although it is found through-  
 564 out the Pacific as shown by our results and the literature (Talley, 2011). PDW encom-  
 565 passes the oldest waters in the Pacific, and are marked by high nitrate and phosphate  
 566 and low oxygen concentrations, as described in Section 3.2 (Östlund & Stuver, 1980; Hau-  
 567 tala & Hammond, 2020). Its highest water mass fractions also clearly follow the silicate  
 568 maximums (Figure S4d).

## 569 4 Discussion

### 570 4.1 Evaluation of model performance

571 The standard deviation of our residuals are 0.3205°C for temperature, 0.1079 for  
 572 salinity, 2.39  $\mu\text{mol kg}^{-1}$  for silicate, 0.91  $\mu\text{mol kg}^{-1}$  for nitrate, 0.05  $\mu\text{mol kg}^{-1}$  for phos-  
 573 phosphate, and 2.36  $\mu\text{mol kg}^{-1}$  for oxygen (Figure S11). Our residuals were highest in the  
 574 thermocline and showed similar patterns among most of the water properties (Figure 8).  
 575 Positive residuals were generally seen in the upper 200 m around 40°N (except for con-  
 576 servative temperature), and negative residuals were seen in the upper 200 m around 50°N  
 577 (except for conservative temperature and salinity). This pattern could be due to influ-  
 578 ence from surface waters not included in our analysis, such as those originating in the

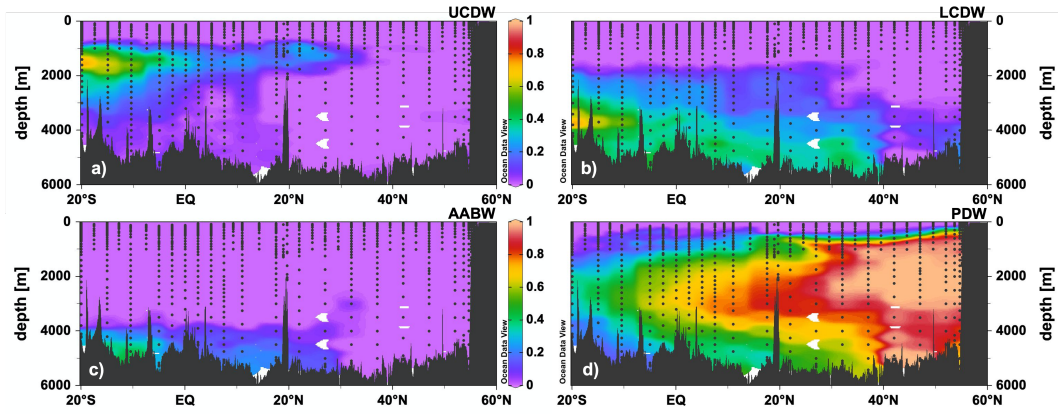


**Figure 7.** Deep water mass fractions for a) UCDW b) LCDW, c) AABW, and d) PDW.

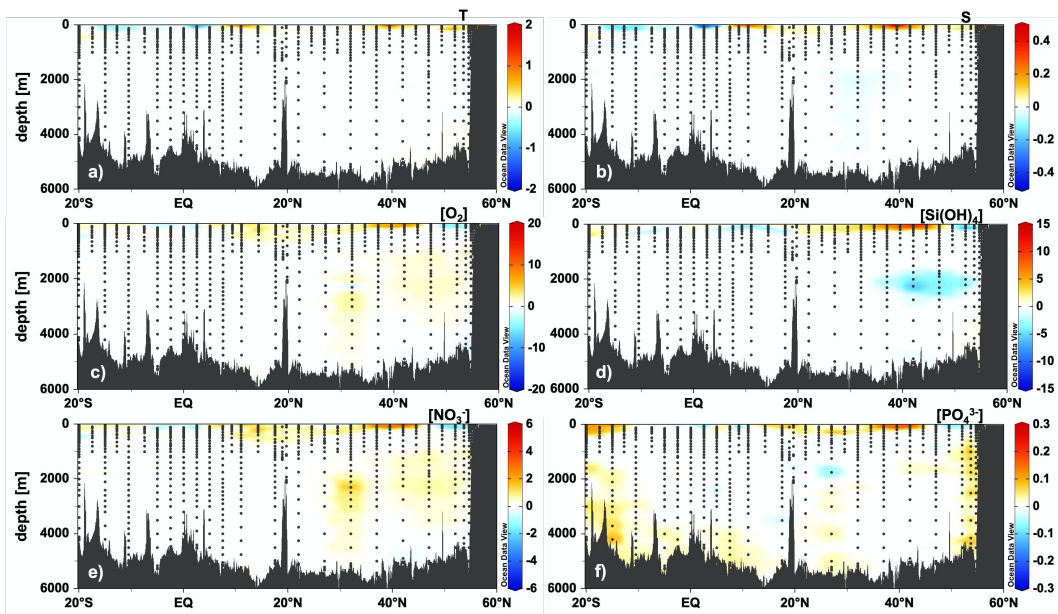


**Figure 8.** Residuals for a) conservative temperature ( $^{\circ}\text{C}$ ) b) absolute salinity, c) oxygen ( $\mu\text{mol kg}^{-1}$ ), d) silicate ( $\mu\text{mol kg}^{-1}$ ), e) nitrate ( $\mu\text{mol kg}^{-1}$ ), and f) phosphate ( $\mu\text{mol kg}^{-1}$ ).

579 Alaska stream, or seasonal and interannual variability in surface and near-surface waters.  
 580 Relatively higher residuals in the upper water column have been observed in other  
 581 OMP analyses, as these water masses are more difficult to define (Jenkins et al., 2015;  
 582 Peters, Jenkins, et al., 2018; García-Ibáñez et al., 2018). Prior analyses also had higher  
 583 residuals near the border separating the intermediate and deep water analyses (Peters,  
 584 Jenkins, et al., 2018). One key difference in our analysis was the strictly enforced wa-  
 585 ter mass conservation. In other analyses, where mass conservation is not met, residu-  
 586 als are generally higher for the other parameters as well (Jenkins et al., 2015; Peters, Jenk-  
 587 ins, et al., 2018). Our average residual is 1% or less of each water property’s range in  
 588 GP15 measurements, comparing well with Artigue et al. (2020). A direct comparison be-  
 589 tween our residuals and the residuals of some past OMP analyses can be found in Fig-  
 590 ure S12 (García-Ibáñez et al., 2018; Peters, Jenkins, et al., 2018; Evans et al., 2020). Over-  
 591 all our residuals were similar to or better than other analyses.

592 Some of the other residuals in our analysis are informative. Between 40°N and 50°N,  
 593 we see patches of relatively large (between -2 and -5  $\mu\text{mol kg}^{-1}$ ) silicate residuals be-  
 594 tween 2000-2500 m (Figure 8). These negative residuals indicate that the chosen water  
 595 mass end members do not explain all of the silicate observed in those samples. This patch  
 596 of residuals lines up with the mid-depth portion of the double silicate maximum found  
 597 in the north Pacific (Edmond et al., 1979; Talley & Joyce, 1992). These residuals are likely  
 598 due to either the treatment of silicate as a conservative parameter (not regenerated) or  
 599 missing end members from the Bering Sea (Hautala & Hammond, 2020). Even so, these  
 600 residuals are a relatively small error for silicate as 5  $\mu\text{mol kg}^{-1}$  corresponds to less than  
 601 3% of the range of GP15 silicate measurements.

602 In addition to our OMP analysis yielding low overall residuals, our solution was  
 603 not sensitive to the parameter weighting chosen for the analysis. The methodology to  
 604 test this was described in Section 2.2.2. The standard deviation of residuals was so low  
 605 (scale of  $10^{-15}$ ) that we can conclude our OMP solution does not change significantly  
 606 with up to 20% changes in parameter weightings (Figure S13).

## 607 4.2 Other water masses relevant to GP15

608 In addition to the water masses described above, Dichothermal water (DtW) (Talley,  
 609 2011; Haley et al., 2014) was observed on our transect, in the subpolar north Pacific at  
 610 the subsurface temperature minimum and oxygen maximum (Section 3.2). These char-  
 611 acteristics are due to its formation via subduction of cold subpolar surface waters. In  
 612 the subarctic gyre, DtW was found between 80-140 m and between  $\sigma_0$  26.2- 26.6  $\text{kg m}^{-3}$   
 613 (Ueno & Yasuda, 2003; Miura et al., 2002). However, within the Alaskan Gyre, DtW was  
 614 identified via elevated oxygen levels found between 30 and 100 m (Haley et al., 2014).  
 615 Alaskan Gyre DtW was described to have a temperature of 3.2°C and a salinity of 32.9  
 616 (Haley et al., 2014). DtW’s characteristic temperature minimum can be seen within our  
 617 PSUW endmember around 26  $\text{kg m}^{-3}$  (Figure S14). Mesothermal water (MtW) is an  
 618 intermediate temperature maximum underneath DTW (Talley, 2011; Ueno & Yasuda,  
 619 2000). We did not observe MtW on GP15, however, which aligns with MtW becoming  
 620 nearly undetectable by fall in the Alaskan Gyre (Ueno & Yasuda, 2000). While Haley  
 621 et al. (2014) identified MtW’s characteristic temperature maximum below DtW in 2007,  
 622 their data were collected between August 19 - September 17, whereas our data were col-  
 623 lected in mid-late September, 2018.

624 North Pacific Central Mode Water (NPCMW) was also likely observed on our tran-  
 625 sect around 35°N (Section 3.2). The WOCE transect, P16, along 152°W found NPCMW  
 626 from 28-35°N and  $\sigma_0$  of 26.2-26.4  $\text{kg m}^{-3}$  (Mecking & Warner, 2001). Ladd and Thomp-  
 627 son (2000) described the formation region of NPCMW around 40°N and 170°E to 160°W  
 628 between 26.0-26.5  $\text{kg m}^{-3}$ , while Oka and Suga (2005) describes NPCMW as being formed  
 629 in the winter between 155-165°E. NPCMW has also been described to have a lighter (25.8-26.2  
 630  $\text{kg m}^{-3}$ ) version formed between the Kuroshio Extension and the Kuroshio Bifurcation  
 631 fronts and a denser (26.3-26.4  $\text{kg m}^{-3}$ ) version formed farther north between the Kuroshio  
 632 Bifurcation and the subarctic fronts (Oka & Suga, 2005). The properties of these ver-  
 633 sions vary year to year, as their properties depend on the adjacent front properties and  
 634 locations that year. Our results find ENPCW and NPIW covering where we would ex-  
 635 pect to see NPCMW (Figure S15). This is likely due to the definitions of both ENPCMW  
 636 and NPIW encompassing NPCMW, with oxygen concentrations of ENPCW around 200  
 637  $\mu\text{mol kg}^{-1}$  at 26  $\text{kg m}^{-3}$  (Figure S14) and NPIW around 268  $\mu\text{mol kg}^{-1}$  (Table S1).

638 North Pacific Eastern Subtropical Mode Water (NPESTMW) was observed on our  
 639 transect above NPCMW. It is commonly identified by a lateral minimum in potential  
 640 vorticity at approximately 30°N, 140°W between  $\sigma_0$  of 24.0-25.4  $\text{kg m}^{-3}$  (Talley, 1988;  
 641 Mecking & Warner, 2001). Along with an oxygen maximum, its properties include a tem-  
 642 perature range of 16.5-22.0 °C and a salinity range of 34.0-35.4 (Hautala & Roemmich,

1998; Katsura, 2018). We likely observed the denser ESTMW ( $24.9 \text{ kg m}^{-3}$ - $25.2 \text{ kg m}^{-3}$ ) on our transect, rather than the lighter version (Katsura, 2018). Denser ESTMW also forms near our transect ( $27$ - $35^\circ\text{N}$ ,  $150$ - $135^\circ\text{W}$ ) from deep winter mixed layers, making it more likely to impact our section. The definition of ENPCW includes NPESTMW because our ENPCW endmember properties between  $24.9$ - $25.2 \text{ kg m}^{-3}$  are about  $200 \mu\text{mol kg}^{-1}$  for  $\text{O}_2$ ,  $19^\circ\text{C}$  for temperature, and a salinity of  $35.25$  (Figure S14). As on earlier occupations of line P16 (Mecking & Warner, 2001), we did not observe North Pacific Subtropical Mode Water (NPSTMW) on the GP15 transect.

Peters, Jenkins, et al. (2018) found the Peruvian ODZ signal to be carried west by the Eastern South Pacific Intermediate Water (ESPIW), which we did not include in our analysis but is likely captured by our SPCW. Indeed, the SPCW appears to capture the signal of the Peruvian ODZ, in our analysis (Figure S16), as seen around  $5^\circ\text{S}$  in the upper  $200$ - $600 \text{ m}$  (Figure 3a). North of the equator, ESSW captures the signal of the Eastern North Pacific ODZ (Figure S17).

Subantarctic Mode Water (SAMW) was also likely observed on our transect via higher oxygen and low silicate (Section 3.2). As in earlier studies (Peters, Jenkins, et al., 2018), our AAIW endmember properties have some overlap with SAMW, and likely encompass it, because SAMW is difficult to distinguish from AAIW north of  $20^\circ\text{S}$  (Tsuchiya & Talley, 1998). This similarity can be seen in the strong similarities between our AAIW endmembers and those of Holte et al. (2013) (Table S2).

The Bering Sea (via the Kamchatka Strait) is a likely source of the high silicate concentrations characteristic of Pacific Deep Water (PDW) (Hautala & Hammond, 2020; Reed et al., 1993). To test this in our study, an alternative PDW definition was chosen from the Bering Sea around the Kamchatka Strait with latitude and longitude ranges of  $55^\circ\text{N}$ - $60^\circ\text{N}$  and  $160^\circ\text{E}$ - $170^\circ\text{E}$ , respectively. The Bering Sea water mass definition is the same as PDW in Table 2 except for the latitude and longitude ranges. The OMP was re-run with the Bering Sea water mass and all water masses previously used except for PDW. This alternate analysis eliminated the low silicate residuals (Figure S18) seen around the silicate mid depth max ( $2000 \text{ m}$  at  $45^\circ\text{N}$  in Figure 8). However, the new residuals for oxygen and nitrate deviated farther from zero below  $3000 \text{ m}$  north of  $40^\circ\text{N}$ . This is likely due to the higher LCDW water mass fractions in this area (Figure S19). Phosphate residuals, primarily in the bottom  $3000 \text{ m}$ , also increased.

## 5 Conclusions

We observed many of the expected features from the central Pacific Ocean in this section, such as warm, salty, and oligotrophic surface waters in the subtropical gyre, the double silicate maximum of PDW, the salinity minima of AAIW and NPIW in their respective hemispheres, and cold, fresh PSUW in the Alaska Gyre. The water mass analysis results align with earlier descriptions of the water masses and the hydrographic and nutrient features of these water masses observed on the transect. Our water mass analysis produced low residuals compared to past studies, indicating that our model describes most of GP15 sample water properties included in the analysis. These results provide a framework for the interpretation of the GEOTRACES GP15 transect data. This product will be especially useful for calculating the expected trace element and isotope (TEI) distributions from water mass mixing along GP15, if the TEI properties for each water type are known.

## Acronyms

**AABW** Antarctic Bottom Water

**AAIW** Antarctic Intermediate Water

**BCO-DMO** Biological and Chemical Oceanography Data Management Office

692 **ENPCW** Eastern North Pacific Central Water  
 693 **ESSW** Equatorial Subsurface Water  
 694 **EqIW** Equatorial Intermediate Water  
 695 **GLODAPv2** Global Ocean Data Analysis Project version 2  
 696 **LCDW** Lower Circumpolar Deep Water  
 697 **NPIW** North Pacific Intermediate Water  
 698 **OCIM** Ocean circulation inverse model  
 699 **OMP** Optimum Multiparameter  
 700 **PDW** Pacific Deep Water  
 701 **PSUW** Pacific Subarctic Upper Water  
 702 **SPCW** South Pacific Central Water  
 703 **SPSTSW** South Pacific Subtropical Surface Water  
 704 **TEI** Trace Elements and Isotopes  
 705 **UCDW** Upper Circumpolar Deep Water

## 706 Acknowledgments

707 The authors thank the captain and crew of R/V Revelle, the seagoing ODF Group  
 708 led by S. Becker, and the GP15 supertechnicians C. Kelly, M. Fleisher, L. Jensen, and B. Sum-  
 709 mers for tireless and outstanding work at sea. We gratefully acknowledge the intellec-  
 710 tual support and leadership from R. Anderson and funding from the U.S. National Sci-  
 711 ence Foundation through grants OCE-1657944 to K. L. Casciotti, OCE-1658318 to P.J.  
 712 Lam, and OCE-1658318 to G. Cutter. The authors declare no competing financial in-  
 713 terests. The manuscript is prepared to comply with the AGU data policy. The datasets  
 714 reported in this study can be found on the BCO-DMO website (<https://www.bco-dmo.org/dataset/778168/data>; <https://www.bco-dmo.org/dataset/777951/data>; and  
 715 <https://www.bco-dmo.org/dataset/824867/data>). The pyompa software can be found  
 716 in Zenodo (<https://zenodo.org/record/5733887>), and the code to replicate the anal-  
 717 ysis can be found in Github (<https://github.com/nitrogenlab/gp15wmanuscripts>). The  
 718 results have been uploaded to the Stanford Digital Repository (<https://purl.stanford.edu/tv301yr5579>) and submitted to BCO-DMO.  
 719  
 720

## 721 References

- 722 Amakawa, H., Nozaki, Y., Alibo, D. S., Zhang, J., Fukugawa, K., & Nagai, H.  
 723 (2004). Neodymium isotopic variations in Northwest Pacific waters. *Geochim-*  
 724 *ica et Cosmochimica Acta*, 68(4), 715–727.  
 725 Anderson, L. A. (1995). On the hydrogen and oxygen content of marine phytoplank-  
 726 ton. *Deep Sea Research Part I: Oceanographic Research Papers*, 42(9), 1675–  
 727 1680.  
 728 Artigue, L., Lacan, F., Van Gennip, S., Lohan, M. C., Wyatt, N. J., Woodward,  
 729 E. M. S., ... Drillet, Y. (2020). Water mass analysis along 22°N in the sub-  
 730 tropical North Atlantic for the JC150 cruise (GEOTRACES, GApr08). *Deep*  
 731 *Sea Research Part I: Oceanographic Research Papers*, 158, 103230.  
 732 Artigue, L., Wyatt, N. J., Lacan, F., Mahaffey, C., & Lohan, M. C. (2021). The  
 733 importance of water mass transport and dissolved-particle interactions on  
 734 the aluminum cycle in the subtropical North Atlantic. *Global Biogeochemical*  
 735 *Cycles*, e2020GB006569.  
 736 Becker, S., Aoyama, M., Woodward, E. M. S., Bakker, K., Coverly, S., Mahaffey, C.,  
 737 & Tanhua, T. (2020). GO-SHIP repeat hydrography nutrient manual: the  
 738 precise and accurate determination of dissolved inorganic nutrients in seawater,  
 739 using continuous flow analysis methods. *Frontiers in Marine Science*, 7, 908.

- 740 Bingham, F. M., & Lukas, R. (1995). The distribution of intermediate water in the  
741 western equatorial Pacific during January–February 1986. *Deep Sea Research*  
742 *Part I: Oceanographic Research Papers*, 42(9), 1545–1573.
- 743 Bograd, S. J., Schroeder, I. D., & Jacox, M. G. (2019). A water mass history of  
744 the Southern California current system. *Geophysical Research Letters*, 46(12),  
745 6690–6698.
- 746 Bostock, H. C., Opdyke, B. N., & Williams, M. J. (2010). Characterising the inter-  
747 mediate depth waters of the Pacific Ocean using  $\delta^{13}\text{C}$  and other geochemical  
748 tracers. *Deep Sea Research Part I: Oceanographic Research Papers*, 57(7),  
749 847–859.
- 750 Bostock, H. C., Sutton, P. J., Williams, M. J., & Opdyke, B. N. (2013). Reviewing  
751 the circulation and mixing of Antarctic Intermediate Water in the South Pa-  
752 cific using evidence from geochemical tracers and Argo float trajectories. *Deep*  
753 *Sea Research Part I: Oceanographic Research Papers*, 73, 84–98.
- 754 Broecker, W. S. (1974). “NO”, a conservative water-mass tracer. *Earth and*  
755 *Planetary Science Letters*, 23(1), 100–107. doi: [https://doi.org/10.1016/0012-](https://doi.org/10.1016/0012-821X(74)90036-3)  
756 [821X\(74\)90036-3](https://doi.org/10.1016/0012-821X(74)90036-3)
- 757 Brown, M. T., Lippiatt, S. M., & Bruland, K. W. (2010). Dissolved aluminum, par-  
758 ticulate aluminum, and silicic acid in northern Gulf of Alaska coastal waters:  
759 Glacial/riverine inputs and extreme reactivity. *Marine Chemistry*, 122(1-4),  
760 160–175.
- 761 Cepeda-Morales, J., Gaxiola-Castro, G., Beier, E., & Godínez, V. M. (2013). The  
762 mechanisms involved in defining the northern boundary of the shallow oxygen  
763 minimum zone in the eastern tropical Pacific Ocean off Mexico. *Deep Sea*  
764 *Research Part I: Oceanographic Research Papers*, 76, 1–12.
- 765 Chang, B. X., Devol, A. H., & Emerson, S. R. (2012). Fixed nitrogen loss from the  
766 eastern tropical North Pacific and Arabian Sea oxygen deficient zones deter-  
767 mined from measurements of  $\text{N}_2$ : Ar. *Global Biogeochemical Cycles*, 26(3).
- 768 Cutler, A., & Breiman, L. (1994, November). Archetypal analysis. *Technometrics*,  
769 36(4), 338–347.
- 770 Cutter, G. A., Casciotti, K. L., & Lam, P. J. (2018). US GEOTRACES Pacific  
771 meridional transect–GP15 cruise report.
- 772 Cutter, G. A., Casciotti, K. L., & Lam, P. J. (2020). *CTD data from the ODF*  
773 *rosette on the US GEOTRACES Pacific Meridional Transect (PMT) cruise*  
774 *(GP15) from September to November 2018*. Biological and Chemical  
775 Oceanography Data Management Office (BCO-DMO). doi: 10.26008/1912/  
776 bco-dmo.778168.2
- 777 Cutter, G. A., Casciotti, K. L., & Lam, P. J. (2021a). *Bottle file from Leg 1 (Seat-*  
778 *tle, WA to Hilo, HI) of the US GEOTRACES Pacific Meridional Transect*  
779 *(PMT) cruise (GP15, RR1814) on R/V Roger Revelle from September to Oc-*  
780 *tober 2018*. Biological and Chemical Oceanography Data Management Office  
781 (BCO-DMO). doi: 10.26008/1912/bco-dmo.777951.6
- 782 Cutter, G. A., Casciotti, K. L., & Lam, P. J. (2021b). *Bottle file from Leg 2 (Hilo,*  
783 *HI to Papeete, French Polynesia) of the US GEOTRACES Pacific Meridional*  
784 *Transect (PMT) cruise (GP15, RR1815) on R/V Roger Revelle from October*  
785 *to November 2018*. Biological and Chemical Oceanography Data Management  
786 Office (BCO-DMO). doi: 10.26008/1912/bco-dmo.824867.5
- 787 Deng, F., Henderson, G. M., Castrillejo, M., Perez, F. F., & Steinfeldt, R. (2018).  
788 Evolution of  $^{231}\text{Pa}$  and  $^{230}\text{Th}$  in overflow waters of the North Atlantic. *Bio-*  
789 *geosciences*, 15(23), 7299–7313.
- 790 Deutsch, C., Gruber, N., Key, R. M., Sarmiento, J. L., & Ganachaud, A. (2001).  
791 Denitrification and  $\text{N}_2$  fixation in the Pacific Ocean. *Global Biogeochemical*  
792 *Cycles*, 15(2), 483–506.
- 793 DeVries, T., & Deutsch, C. (2014). Large-scale variations in the stoichiometry of  
794 marine organic matter respiration. *Nature Geoscience*, 7(12), 890–894.

- 795 Edmond, J., Jacobs, S., Gordon, A., Mantyla, A., & Weiss, R. (1979). Water column  
796 anomalies in dissolved silica over opaline pelagic sediments and the origin of  
797 the deep silica maximum. *Journal of Geophysical Research: Oceans*, *84*(C12),  
798 7809–7826.
- 799 Emery, W., & Meincke, J. (1986). Global water masses: summary and review.  
800 *Oceanologica Acta*, *9*(4), 383–391.
- 801 Evans, N., Boles, E., Kwiecinski, J. V., Mullen, S., Wolf, M., Devol, A. H., ... Mof-  
802 fett, J. W. (2020). The role of water masses in shaping the distribution of  
803 redox active compounds in the Eastern Tropical North Pacific oxygen deficient  
804 zone and influencing low oxygen concentrations in the eastern Pacific Ocean.  
805 *Limnology Oceanography*, *65*(8), 1688–1705.
- 806 Faure, V., & Speer, K. (2012). Deep circulation in the eastern South Pacific Ocean.  
807 *Journal of Marine Research*, *70*(5), 748–778.
- 808 Fiedler, P. C., & Talley, L. D. (2006). Hydrography of the eastern tropical Pacific: A  
809 review. *Progress in Oceanography*, *69*(2-4), 143–180.
- 810 García-Ibáñez, M. I., Pérez, F. F., Lherminier, P., Zunino, P., Mercier, H., &  
811 Tréguer, P. (2018). Water mass distributions and transports for the 2014  
812 GEOVIDE cruise in the North Atlantic. *Biogeosciences*, *15*(7), 2075–2090.
- 813 Georgi, D. T. (1979). Modal properties of Antarctic Intermediate Water in the  
814 southeast Pacific and the South Atlantic. *Journal of Physical Oceanography*,  
815 *9*(3), 456–468.
- 816 GEOTRACES. (n.d.). *GEOTRACES quality flag policy*.  
817 <https://www.geotraces.org/geotraces-quality-flag-policy/>.
- 818 GEOTRACES Intermediate Data Product Group. (2021). *The GEOTRACES In-*  
819 *termediate Data Product 2021 (IDP2021)*. NERC EDS British Oceanographic  
820 Data Centre NOC. doi: 10.5285/cf2d9ba9-d51d-3b7c-e053-8486abc0f5fd
- 821 GEOTRACES Science Planning Group. (2006). *GEOTRACES science plan*. Scien-  
822 tific Committee on Oceanic Research. Baltimore, Maryland.
- 823 Gruber, N., & Sarmiento, J. L. (1997). Global patterns of marine nitrogen fixation  
824 and denitrification. *Global Biogeochemical Cycles*, *11*(2), 235–266.
- 825 Haley, B. A., Frank, M., Hathorne, E., & Pisias, N. (2014). Biogeochemical impli-  
826 cations from dissolved rare earth element and Nd isotope distributions in the  
827 Gulf of Alaska. *Geochimica et Cosmochimica Acta*, *126*, 455–474.
- 828 Hartin, C. A., Fine, R. A., Sloyan, B. M., Talley, L. D., Chereskin, T. K., & Hap-  
829 pell, J. (2011). Formation rates of Subantarctic mode water and Antarctic  
830 intermediate water within the South Pacific. *Deep Sea Research Part I: Oceanographic Research Papers*, *58*(5), 524–534.
- 831 Hautala, S. L., & Hammond, D. E. (2020). Abyssal pathways and the double Sil-  
832 ica maximum in the Northeast Pacific Basin. *Geophysical Research Letters*,  
833 *47*(19), e2020GL089010.
- 834 Hautala, S. L., & Roemmich, D. H. (1998). Subtropical mode water in the North-  
835 east Pacific Basin. *Journal of Geophysical Research: Oceans*, *103*(C6), 13055–  
836 13066.
- 837 Holte, J. W., Talley, L. D., Chereskin, T. K., & Sloyan, B. M. (2013). Subantarctic  
838 mode water in the southeast Pacific: Effect of exchange across the Subantarctic  
839 Front. *Journal of Geophysical Research: Oceans*, *118*(4), 2052–2066.
- 840 Holzer, M., DeVries, T., & de Laverne, C. (2021). Diffusion controls the ventilation  
841 of a Pacific Shadow Zone above abyssal overturning. *Nature Communications*,  
842 *12*(1), 1–13.
- 843 Hou, Y., Hammond, D. E., Berelson, W. M., Kemnitz, N., Adkins, J. F., & Lun-  
844 strum, A. (2019). Spatial patterns of benthic silica flux in the North Pacific  
845 reflect upper ocean production. *Deep Sea Research Part I: Oceanographic Research Papers*, *148*, 25–33.
- 846 Hu, W., Chen, M., Yang, W., Zhang, R., Qiu, Y., & Zheng, M. (2014). Enhanced  
847 particle scavenging in deep water of the Aleutian Basin revealed by 210Po-  
848  
849

- 210Pb disequilibria. *Journal of Geophysical Research: Oceans*, 119(6), 3235–3248.
- Iudicone, D., Rodgers, K. B., Schopp, R., & Madec, G. (2007). An exchange window for the injection of Antarctic Intermediate Water into the South Pacific. *Journal of Physical Oceanography*, 37(1), 31–49.
- Jenkins, W., Hatta, M., Fitzsimmons, J., Schlitzer, R., Lanning, N., Shiller, A., . . . others (2020). An intermediate-depth source of hydrothermal  $^3\text{He}$  and dissolved iron in the North Pacific. *Earth and Planetary Science Letters*, 539, 116223.
- Jenkins, W., Smethie Jr, W., Boyle, E., & Cutter, G. (2015). Water mass analysis for the US GEOTRACES (GA03) North Atlantic sections. *Deep Sea Research Part II: Topical Studies in Oceanography*, 116, 6–20.
- Katsura, S. (2018). Properties, formation, and dissipation of the North Pacific Eastern Subtropical Mode Water and its impact on interannual spiciness anomalies. *Progress in Oceanography*, 162, 120–131.
- Kawabe, M., & Fujio, S. (2010). Pacific Ocean circulation based on observation. *Journal of Oceanography*, 66(3), 389–403.
- Key, R. M., Olsen, A., van Heuven, S., Lauvset, S. K., Velo, A., Lin, X., . . . others (2015). Global ocean data analysis project, version 2 (GLODAPv2). *ORNL/CDIAC-162, NDP-093*.
- Kim, I.-N., Min, D.-H., & Macdonald, A. M. (2013). Water column denitrification rates in the oxygen minimum layer of the Pacific Ocean along 32°S. *Global Biogeochemical Cycles*, 27(3), 816–827.
- Ladd, C., & Thompson, L. A. (2000). Formation mechanisms for North Pacific central and eastern subtropical mode waters. *Journal of Physical Oceanography*, 30(5), 868–887.
- Lam, P. J., Bishop, J. K., Henning, C. C., Marcus, M. A., Waychunas, G. A., & Fung, I. Y. (2006). Wintertime phytoplankton bloom in the subarctic Pacific supported by continental margin iron. *Global Biogeochemical Cycles*, 20(1).
- Lauvset, S. K., Lange, N., Tanhua, T., Bittig, H. C., Olsen, A., Kozyr, A., . . . others (2021). An updated version of the global interior ocean biogeochemical data product, GLODAPv2. 2021. *Earth System Science Data Discussions*, 1–32.
- Lee, S.-K., Lumpkin, R., Baringer, M. O., Meinen, C. S., Goes, M., Dong, S., . . . Yeager, S. G. (2019). Global meridional overturning circulation inferred from a data-constrained ocean & sea-ice model. *Geophysical Research Letters*, 46(3), 1521–1530.
- Lehmann, N., Kienast, M., Granger, J., Bourbonnais, A., Altabet, M., & Tremblay, J.-É. (2019). Remote western Arctic nutrients fuel remineralization in deep Baffin Bay. *Global Biogeochemical Cycles*, 33(6), 649–667.
- Le Roy, E., Sanial, V., Charette, M. A., Beek, P. v., Lacan, F., Jacquet, S. H., . . . others (2018). The 226 Ra–Ba relationship in the North Atlantic during GEOTRACES-GA01. *Biogeosciences*, 15(9), 3027–3048.
- Mahoney, J., Sinton, J., Kurz, M., Macdougall, J., Spencer, K., & Lugmair, G. (1994). Isotope and trace element characteristics of a super-fast spreading ridge: East Pacific Rise, 13–23°S. *Earth and Planetary Science Letters*, 121(1–2), 173–193.
- Marshall, J., Donohoe, A., Ferreira, D., & McGee, D. (2014). The ocean’s role in setting the mean position of the Inter-Tropical Convergence Zone. *Climate Dynamics*, 42(7), 1967–1979.
- McCartney, M. S. (1977). Subantarctic Mode Water. In M. V. Angel (Ed.), *A voyage of discovery: George Deacon 70th anniversary volume* (Supplement to Deep-Sea Research ed., pp. 103–119). Oxford: Pergamon Press.
- Measures, C., Henderson, G., Anderson, R., Adkins, J., Andersson, P., Boyle, E., . . . Zhang, J. (2007). GEOTRACES—An international study of the global marine biogeochemical cycles of trace elements and their isotopes. *Geochemistry*,

- 67(2), 85–131.
- 905 Mecking, S., & Warner, M. J. (2001). On the subsurface CFC maxima in the  
 906 subtropical North Pacific thermocline and their relation to mode waters and  
 907 oxygen maxima. *Journal of Geophysical Research: Oceans*, 106(C10), 22179–  
 908 22198.
- 909 Miura, T., Suga, T., & Hanawa, K. (2002). Winter mixed layer and formation of  
 910 dichothermal water in the Bering Sea. *Journal of Oceanography*, 58(6), 815–  
 911 823.
- 912 Molinelli, E. J. (1981). The Antarctic influence on Antarctic Intermediate Water.  
 913 *Journal of Marine Research*, 39, 267–293.
- 914 Montes, I., Dewitte, B., Gutknecht, E., Paulmier, A., Dadou, I., Oschlies, A., &  
 915 Garçon, V. (2014). High-resolution modeling of the Eastern Tropical Pacific  
 916 oxygen minimum zone: Sensitivity to the tropical oceanic circulation. *Journal*  
 917 *of Geophysical Research: Oceans*, 119(8), 5515–5532.
- 918 Musgrave, D. L., Weingartner, T. J., & Royer, T. C. (1992). Circulation and hydrog-  
 919 raphy in the northwestern Gulf of Alaska. *Deep Sea Research Part A. Oceanog-  
 920 raphic Research Papers*, 39(9), 1499–1519.
- 921 Nameroff, T., Balistreri, L., & Murray, J. (2002). Suboxic trace metal geochem-  
 922 istry in the eastern tropical North Pacific. *Geochimica et Cosmochimica Acta*,  
 923 66(7), 1139–1158.
- 924 Oka, E., & Suga, T. (2005). Differential formation and circulation of North Pacific  
 925 central mode water. *Journal of Physical Oceanography*, 35(11), 1997–2011.
- 926 Olsen, A., Key, R. M., Van Heuven, S., Lauvset, S. K., Velo, A., Lin, X., . . . others  
 927 (2016). The Global Ocean Data Analysis Project version 2 (GLODAPv2)—an  
 928 internally consistent data product for the world ocean. *Earth System Science*  
 929 *Data*, 8(2), 297–323.
- 930 Orsi, A. H., Johnson, G. C., & Bullister, J. L. (1999). Circulation, mixing, and pro-  
 931 duction of Antarctic Bottom Water. *Progress in Oceanography*, 43(1), 55–109.
- 932 Orsi, A. H., Whitworth III, T., & Nowlin Jr, W. D. (1995). On the meridional ex-  
 933 tent and fronts of the Antarctic Circumpolar Current. *Deep Sea Research Part*  
 934 *I: Oceanographic Research Papers*, 42(5), 641–673.
- 935 Östlund, H., & Stuiver, M. (1980). GEOSECS Pacific radiocarbon. *Radiocarbon*,  
 936 22(1), 25–53.
- 937 Peters, B. D., Jenkins, W. J., Swift, J. H., German, C. R., Moffett, J. W., Cutter,  
 938 G. A., . . . Casciotti, K. L. (2018). Water mass analysis of the 2013 US GEO-  
 939 TRACES eastern Pacific zonal transect (GP16). *Marine Chemistry*, 201,  
 940 6–19.
- 941 Peters, B. D., Lam, P. J., & Casciotti, K. L. (2018). Nitrogen and oxygen isotope  
 942 measurements of nitrate along the US GEOTRACES Eastern Pacific Zonal  
 943 Transect (GP16) yield insights into nitrate supply, remineralization, and water  
 944 mass transport. *Marine Chemistry*, 201, 137–150.
- 945 Piola, A. R., & Georgi, D. T. (1982). Circumpolar properties of Antarctic intermedi-  
 946 ate water and Subantarctic Mode Water. *Deep Sea Research Part A. Oceanog-  
 947 raphic Research Papers*, 29(6), 687–711.
- 948 Rafter, P. A., DiFiore, P. J., & Sigman, D. M. (2013). Coupled nitrate nitrogen  
 949 and oxygen isotopes and organic matter remineralization in the Southern and  
 950 Pacific Oceans. *Journal of Geophysical Research: Oceans*, 118(10), 4781–4794.
- 951 Reed, R., Khen, G., Stabeno, P., & Verkhunov, A. (1993). Water properties  
 952 and flow over the deep Bering Sea basin, summer 1991. *Deep Sea Re-  
 953 search Part I: Oceanographic Research Papers*, 40(11), 2325–2334. doi:  
 954 [https://doi.org/10.1016/0967-0637\(93\)90107-E](https://doi.org/10.1016/0967-0637(93)90107-E)
- 955 Reid, J. L. (1965). Intermediate waters of the Pacific Ocean. *The Johns Hopkins*  
 956 *Oceanographic Studies*.
- 957 Reid, J. L. (1997). On the total geostrophic circulation of the Pacific Ocean: Flow  
 958 patterns, tracers, and transports. *Progress in Oceanography*, 39(4), 263–352.
- 959

- 960 Roshan, S., & Wu, J. (2015). Water mass mixing: The dominant control on the zinc  
961 distribution in the North Atlantic Ocean. *Global Biogeochemical Cycles*, *29*(7),  
962 1060–1074.
- 963 Royer, T. C. (1979). On the effect of precipitation and runoff on coastal circulation  
964 in the Gulf of Alaska. *Journal of Physical Oceanography*, *9*(3), 555–563.
- 965 Sarmiento, J. L. (2013). Organic matter export and remineralization. In *Ocean bio-*  
966 *geochemical dynamics* (pp. 173–226). Princeton University Press.
- 967 Schmitz Jr, W. J. (1996). *On the World Ocean Circulation. Volume 1. Some Global*  
968 *Features/North Atlantic Circulation*. (Tech. Rep. No. WHOI-96-0B). Woods  
969 Hole, MA: Woods Hole Oceanographic Institution.
- 970 Schroeder, I. D., Santora, J. A., Bograd, S. J., Hazen, E. L., Sakuma, K. M., Moore,  
971 A. M., . . . Field, J. C. (2019). Source water variability as a driver of rock-  
972 fish recruitment in the California Current Ecosystem: Implications for climate  
973 change and fisheries management. *Canadian Journal of Fisheries and Aquatic*  
974 *Sciences*, *76*(6), 950–960.
- 975 SeaDataNet. (2010, May). Data quality control procedures (2.0 ed.) [Computer soft-  
976 ware manual].
- 977 Seckel, G. R. (1968). A time-sequence oceanographic investigation in the North Pa-  
978 cific trade-wind zone. *Eos, Transactions American Geophysical Union*, *49*(1),  
979 377–387.
- 980 Sedwick, P. N., McMurtry, G., & Macdougall, J. (1992). Chemistry of hydrother-  
981 mal solutions from Pele’s vents, Loihi Seamount, Hawaii. *Geochimica et Cos-*  
982 *mochimica Acta*, *56*(10), 3643–3667.
- 983 Shrikumar, A., Lawrence, R., & Casciotti, K. L. (2022). PYOMPA technical note.  
984 Retrieved from [essoar.org/doi/10.1002/essoar.10507053.4](https://essoar.org/doi/10.1002/essoar.10507053.4)
- 985 Silva, N., Rojas, N., & Fedele, A. (2009). Water masses in the Humboldt Current  
986 System: Properties, distribution, and the nitrate deficit as a chemical water  
987 mass tracer for Equatorial Subsurface Water off Chile. *Deep Sea Research Part*  
988 *II: Topical Studies in Oceanography*, *56*(16), 1004–1020.
- 989 Sloyan, B. M., & Rintoul, S. R. (2001). Circulation, renewal, and modification of  
990 Antarctic Mode and Intermediate Water. *Journal of Physical Oceanography*,  
991 *31*(4), 1005–1030.
- 992 Sprintall, J., & Tomczak, M. (1993). On the formation of Central Water and ther-  
993 moclone ventilation in the southern hemisphere. *Deep Sea Research Part I:*  
994 *Oceanographic Research Papers*, *40*(4), 827–848.
- 995 Stramma, L., Johnson, G. C., Firing, E., & Schmidtko, S. (2010). Eastern Pacific  
996 oxygen minimum zones: Supply paths and multidecadal changes. *Journal of*  
997 *Geophysical Research: Oceans*, *115*(C9).
- 998 Sverdrup, H. U., Johnson, M. W., Fleming, R. H., et al. (1942). *The oceans: Their*  
999 *physics, chemistry, and general biology* (Vol. 1087). Prentice-Hall New York.
- 1000 Talley, L. D. (1988). Potential vorticity distribution in the North Pacific. *Journal of*  
1001 *Physical Oceanography*, *18*(1), 89–106.
- 1002 Talley, L. D. (1993). Distribution and formation of North Pacific intermediate water.  
1003 *Journal of Physical Oceanography*, *23*(3), 517–537.
- 1004 Talley, L. D. (2011). *Descriptive physical oceanography: An introduction*. Academic  
1005 Press.
- 1006 Talley, L. D. (2013). Closure of the global overturning circulation through the In-  
1007 dian, Pacific, and Southern Oceans: Schematics and transports. *Oceanography*,  
1008 *26*(1), 80–97.
- 1009 Talley, L. D., & Joyce, T. M. (1992). The double silica maximum in the North Pa-  
1010 cific. *Journal of Geophysical Research: Oceans*, *97*(C4), 5465–5480.
- 1011 Talley, L. D., Joyce, T. M., & Deszoeke, R. A. (1991). Transpacific sections at 47  
1012 N and 152 W: distribution of properties. *Deep Sea Research Part A. Ocean-*  
1013 *ographic Research Papers*, *38*, S63–S82.
- 1014 Talley, L. D., Nagata, Y., Fujimura, M., Iwao, T., Kono, T., Inagake, D., . . . Okuda,

- 1015 K. (1995). North Pacific intermediate water in the Kuroshio/Oyashio mixed  
1016 water region. *Journal of Physical Oceanography*, *25*(4), 475–501.
- 1017 Teng, Y.-C., Primeau, F. W., Moore, J. K., Lomas, M. W., & Martiny, A. C. (2014).  
1018 Global-scale variations of the ratios of carbon to phosphorus in exported ma-  
1019 rine organic matter. *Nature Geoscience*, *7*(12), 895–898.
- 1020 Thomson, R. E., & Krassovski, M. V. (2010). Poleward reach of the California Un-  
1021 dercurrent extension. *Journal of Geophysical Research: Oceans*, *115*(C9).
- 1022 Tomczak, M. (1981, January). A multi-parameter extension of temperature/salinity  
1023 diagram techniques for the analysis of non-isopycnal mixing. *Prog. Oceanogr.*,  
1024 *10*(3), 147–171.
- 1025 Tomczak, M., & Godfrey, J. (2003a). Hydrology of the Pacific Ocean. In *Regional*  
1026 *oceanography: An introduction* (chap. 9). New Delhi, India: Daya Publishing  
1027 House.
- 1028 Tomczak, M., & Godfrey, J. S. (2003b). *Regional oceanography: An introduction*.  
1029 New Delhi, India: Daya Publishing House.
- 1030 Tomczak, M., & Liefvink, S. (2005). Interannual variations of water mass volumes in  
1031 the Southern Ocean. *Journal of Atmospheric & Ocean Science*, *10*(1), 31–42.
- 1032 Trefry, J. H., Butterfield, D. B., Metz, S., Massoth, G. J., Trocine, R. P., & Feely,  
1033 R. A. (1994). Trace metals in hydrothermal solutions from Cleft segment  
1034 on the southern Juan de Fuca Ridge. *Journal of Geophysical Research: Solid*  
1035 *Earth*, *99*(B3), 4925–4935.
- 1036 Tsuchiya, M., & Talley, L. D. (1998). A Pacific hydrographic section at 88°W:  
1037 Water-property distribution. *Journal of Geophysical Research: Oceans*,  
1038 *103*(C6), 12899–12918.
- 1039 Ueno, H., & Yasuda, I. (2000). Distribution and formation of the mesothermal struc-  
1040 ture (temperature inversions) in the North Pacific subarctic region. *Journal of*  
1041 *Geophysical Research: Oceans*, *105*(C7), 16885–16897.
- 1042 Ueno, H., & Yasuda, I. (2003). Intermediate water circulation in the North Pacific  
1043 subarctic and northern subtropical regions. *Journal of Geophysical Research:*  
1044 *Oceans*, *108*(C11).
- 1045 Van Scoy, K. A., Olson, D. B., & Fine, R. A. (1991). Ventilation of North Pacific  
1046 intermediate waters: The role of the Alaskan gyre. *Journal of Geophysical Re-*  
1047 *search: Oceans*, *96*(C9), 16801–16810.
- 1048 Whitworth III, T., Orsi, A., Kim, S.-J., Nowlin Jr, W., & Locarnini, R. (1985, Jan-  
1049 uary). Ocean, ice, and atmosphere: Interactions at the Antarctic continental  
1050 margin. In S. S. Jacobs & R. F. Weiss (Eds.), (Vol. 75, pp. 1–27). Washington,  
1051 D.C.: American Geophysical Union. (<https://doi.org/10.1029/AR075p0001>)
- 1052 Wyrski, K. (1967). Circulation and water masses in the eastern equatorial Pacific  
1053 Ocean. *International Journal of Oceanology & Limnology*, *1*(2), 117–147.
- 1054 Yamagishi, H., Westley, M. B., Popp, B. N., Toyoda, S., Yoshida, N., Watanabe,  
1055 S., ... Yamanaka, Y. (2007). Role of nitrification and denitrification on the  
1056 nitrous oxide cycle in the eastern tropical North Pacific and Gulf of California.  
1057 *Journal of Geophysical Research: Biogeosciences*, *112*(G2).
- 1058 Yasuda, I. (1997). The origin of the North Pacific intermediate water. *Journal of*  
1059 *Geophysical Research: Oceans*, *102*(C1), 893–909.
- 1060 You, Y., Sugimoto, N., Fukasawa, M., Yasuda, I., Kaneko, I., Yoritaka, H., &  
1061 Kawamiya, M. (2000). Roles of the Okhotsk Sea and Gulf of Alaska in form-  
1062 ing the North Pacific intermediate water. *Journal of Geophysical Research:*  
1063 *Oceans*, *105*(C2), 3253–3280.
- 1064 You, Y., Sugimoto, N., Fukasawa, M., Yoritaka, H., Mizuno, K., Kashino, Y., &  
1065 Hartoyo, D. (2003). Transport of North Pacific intermediate water across  
1066 Japanese WOCE sections. *Journal of Geophysical Research: Oceans*, *108*(C6).
- 1067 Yuan, X., & Talley, L. D. (1992). Shallow salinity minima in the North Pacific.  
1068 *Journal of Physical Oceanography*, *22*(11), 1302–1316.

# Supporting Information for Water mass analysis of the 2018 US GEOTRACES Pacific Meridional Transect (GP15)

R. M. Lawrence <sup>1</sup>, A. Shrikumar <sup>1</sup>, E. Le Roy <sup>2</sup>, J. Swift <sup>3</sup>, P. J. Lam <sup>4</sup>, G. Cutter <sup>5</sup>, and K. L. Casciotti <sup>1</sup>

<sup>1</sup>Department of Earth System Science, Stanford University, Stanford, CA, USA

<sup>2</sup>Department of Marine Chemistry and Geochemistry, Woods Hole Oceanographic Institution, Woods Hole, MA, USA

<sup>3</sup>Department of Climate, Atmospheric Science, and Physical Oceanography, Scripps Institution of Oceanography, La Jolla, CA 92037, USA

<sup>4</sup>University of California, Santa Cruz, Department of Ocean Sciences, 1156 High St, Santa Cruz, CA 95064, USA

<sup>5</sup>Department of Ocean and Earth Sciences, Old Dominion University, Norfolk, VA 23529, USA

## Contents of this file

1. Text S1 to S4
2. Figures S1 to S19
3. Tables S1 to S2

## Introduction

This document contains supporting text, figures, and tables containing additional information and detail cited in the main text. The GP15 datasets used can be found on the BCO-DMO website (<https://www.bco-dmo.org/dataset/778168/>)

---

data; <https://www.bco-dmo.org/dataset/777951/data>; <https://www.bco-dmo.org/dataset/824867/data>). Only data collected by the Oceanographic Data Facility (ODF, Scripps Institution of Oceanography) group was used. The water mass analysis results have been upload to the Stanford Digital Repository (<https://purl.stanford.edu/tv301yr5579>) and submitted to BCO-DMO. The water mass analysis was conducted via a modified Optimum Multiparameter (OMP) analysis method using the before-mentioned BCO-DMO GP15 datasets and the newly-developed pyompa package. The pyompa software can be found in Zenodo (<https://zenodo.org/record/5733887>), and the code to replicate the analysis can be found in Github (<https://github.com/nitrogenlab/gp15wmascripts>). Any known anomalies in the BCO-DMO datasets were flagged according to the SeaDataNet scheme as is recommended by GEOTRACES (SeaDataNet, 2010; GEOTRACES, n.d.; Cutter et al., 2018). Our analysis excluded data flagged as missing or as a known bad value. Once these data were removed, the thermocline (n=341) and intermediate/deep (n=682) samples with complete data for our parameters of interest (Section 2.2.1) were analyzed.

**Text S1.** pyompa soft penalty formulation.

The formula for the soft penalties applied to constrain the OMPA is below.

$$penalty(x) = \beta(e^{\alpha \max(0, \max(lowerbound - x, x - upperbound))} - 1)$$

The 'lowerbound' and 'upperbound' refer to the range over which each penalty is set. In this case, a specific latitude or potential density. The default  $\alpha$  and  $\beta$  for latitude and potential density penalties were  $\alpha = 0.05$  and  $\beta = 100$ . These default values were used except in the following cases. In the intermediate and deep water analysis, ENPCW, SPCW, PSUW, ESSW, EqIW, and AAIW, had  $\alpha = 0.03$  and  $\beta = 50$  for their respective

latitude penalties. In the thermocline analysis, only PSUW and SPCW deviated from the default with  $\alpha = 0.03$  and  $\beta = 50$  for their respective latitude latitude penalties.

**Text S2.** Parameter weightings

Our parameter weightings were modified from Peters et al. (2018) as follows. In the thermocline, we started with Peters et al. (2018)'s coded weights of 160, 155, 5, and 10 for temperature, salinity, silicate, and PO (a combination of phosphate and oxygen), respectively. Oxygen was given the same weight as PO, and we weighted phosphate five times the weight of oxygen to give its contribution to the overall cost a similar magnitude. Nitrate was given the same weight as phosphate. We also increased the weight of temperature by 25%. After dividing all the weights by ten to lower the overall weights while maintaining the relative weighting, the weights applied to the thermocline OMP analysis were 20.0, 15.5, 0.5, 5, 5, and 1 for conservative temperature, salinity,  $\text{Si}(\text{OH})_4$ ,  $\text{NO}_3^-$ ,  $\text{PO}_4^{3-}$ , and  $\text{O}_2$ , respectively.

In the intermediate and deep waters, we started with Peters et al. (2018)'s coded weights of 140, 100, 30, and 10 for temperature, salinity, silicate, and NO (a combination of nitrate and oxygen). Oxygen was given the same weight as NO, and we weighted nitrate five times the weight of oxygen to give its contribution to the overall cost a similar magnitude. Phosphate was given the same weight as nitrate. We also increased the weight of temperature and salinity to account for their conservative nature compared to the other parameters affected by particle dissolution and nutrient regeneration. After dividing all the weights by ten, as described above, intermediate and deep OMP analysis weights were of 56, 80, 3, 5, 5, and 1 for conservative temperature, salinity,  $\text{Si}(\text{OH})_4$ ,  $\text{NO}_3^-$ ,  $\text{PO}_4^{3-}$ , and  $\text{O}_2$ , respectively.

We compared our parameter weightings to weights cited in (Peters et al., 2018), which are 140 for temperature, 100 for salinity, 30 for silicate, 20 for NO, and 10 for PO. We translated the weights of PO and NO as 20 for oxygen, 20 for nitrate, and 10 for phosphate. These (Peters et al., 2018) weights were kept the same in both the thermocline and intermediate and deep water analyses. The differences in water mass fractions between these GP15 water mass analyses (our water mass fractions minus the water mass fractions resulting from (Peters et al., 2018)'s cited weights) is in figures S2 and S3.

**Text S3.** Procedure for obtaining thermocline boundaries

Because observations in the thermocline are analyzed using the "thermocline array" technique while observations in the intermediate and deep waters are analyzed with the standard pyompa technique, it is important to separate the observations in the thermocline from those that are in intermediate and deep waters. In prior work (Peters et al., 2018; Jenkins et al., 2015), a single cutoff in potential density was applied across all observations to separate out those in the thermocline. However, in reality, the end of the true thermocline may exist at different potential density cutoffs depending on the station being considered. To account for this, in this work we determined station-specific thermocline thresholds as follows:

First, we downloaded the GP15 ODF CTD data from the BCO-DMO website (<https://www.bco-dmo.org/dataset/778168/data>) and organized the observations by station. In cases where there were multiple CTD casts per station, we focused on data from the cast that had more observations. Then, for each station, we followed these steps:

1. Organize the data for the station into two vectors: the first vector contains the depths of the observations sorted in ascending order, and the second vector contains the corresponding potential density values (set to a reference depth of 0 m).

2. Density should increase monotonically with depth, but sometimes slight noise in the observations can cause density to appear to decrease with increasing depth. To get around this, we use a technique called "isotonic regression", where we fit a non-decreasing function where the input is the depth and the output is the potential density. To fit the isotonic regressor, we used scikit learn's Isotonic Regression class (<https://scikit-learn.org/stable/modules/isotonic.html>).

3. Isotonic regression produces a non-smooth function that increases in sharp steps. To create a smoothed version of the output of the isotonic regressor, we fit the output of the isotonic regressor to a PCHIP interpolator (PCHIP stands for "Piecewise Cubic Hermite Interpolating Polynomial"), as implemented by scipy (<https://docs.scipy.org/doc/scipy/reference/generated/scipy.interpolate.PchipInterpolator.html>). The PCHIP interpolator produces a smooth fit while preserving the monotonicity of the isotonic regressor. We will use  $\sigma_0$  to denote the function produced by the PCHIP interpolator, such that the potential density output for a depth  $z$  is written as  $\sigma_0(z)$ .

4. Once we have the smooth piecewise polynomial function  $\sigma_0$ , we can calculate its first derivative at any depth. We will use  $\sigma'_0(z)$  to denote the first derivative of the potential density at a depth  $z$ . We compute this derivative at 1000 evenly-spaced depths between the minimum and maximum depths of the observations at the station.

5. To identify a cutoff for the thermocline (or, more formally, the pycnocline), we make the simplifying assumption that the gradient of the potential density is first monotonically

increasing (i.e. the gradient gets steeper and steeper as we enter the thermocline), and is then monotonically decreasing (i.e. gets less steep as we exit the thermocline and enter the abyssal ocean). Although this assumption is not always true in practice (e.g. the presence of a mode water can create a flatness in the density gradient before the abyssal waters are reached), for our purposes of identifying the upper and lower boundaries of the thermocline, we find that it is sufficient. To put this assumption into practice, we find the maximum of the derivative (over the 1000 depths mentioned in the previous steps), and then split the 1000 depths into two sections around this maximum. For the shallower section, we fit a monotonically increasing isotonic regressor to the values of  $\sigma'(z)$  (call the resulting function  $\sigma'_{inc}$ ), and for the deeper section we fit a monotonically decreasing isotonic regressor (call the result function  $\sigma'_{dec}$ ).

6. The upper thermocline boundary is set at which  $\sigma'_{inc}(z)$  is either  $\geq 0.01$  or is  $\geq 25\%$  of the maximum derivative (over the 1000 depths), whichever was shallower. We define the lower boundary of the thermocline as the depth in the deeper section at which  $\sigma'_{dec}(z) \leq 0.003$ . These cutoffs were chosen based on visual inspection, and will likely need to be adjusted for different datasets.

After performing the procedure above for all stations, we have upper and lower bounds for the thermocline for each station (Figure S3).

#### **Text S4.** Thermocline endmember selection

In the thermocline array technique, different end-members are defined for every potential density increment. How do we define the property values for these end-members? To achieve this, we combined the cubic smoothing splines approach used in Jenkins et al. (2015) and Peters et al. (2018) with a novel iterative outlier filtering scheme as follows:

first, we downloaded GLODAPv2 data for the Pacific and Arctic oceans and combined them into one dataset. Next, we used the ranges from Table 1 to filter for datapoints corresponding to a particular end-member. Then, for each property value, we go through the datapoints corresponding to each single end-member and fit a cubic spline as follows:

1. Fit a cubic smoothing spline to predict the value of the property as a function of the potential density (reference depth 0 m). We used the csaps python package (<https://github.com/espdev/csaps>) version 1.1.0, with the smoothing parameter  $p$  set to 0.8.

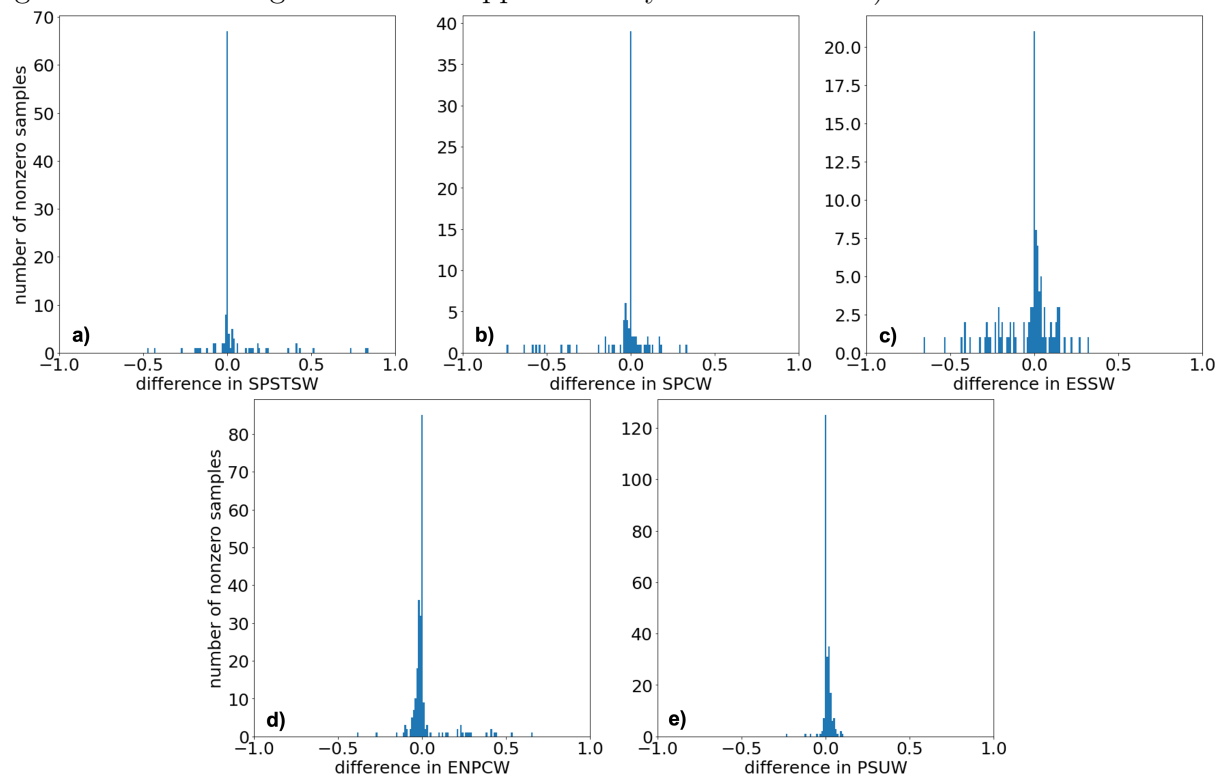
2. Look at all the datapoints corresponding to the end-member and we compute the difference between the true property value and the predicted property value according to the csaps spline from the previous step. We then square these errors, compute the standard deviation, and filter out all datapoints for which the square of the residual is more than two standard deviations greater than zero.

3. Recompute a new smoothing spline on the filtered dataset, and recompute which points would be filtered out according to the new spline. If the set of points getting filtered out is the same as before, end the iteration and designate the newly computed cubic spline as the final cubic spline. Otherwise, repeat this step, but now filtering out points based on the new spline.

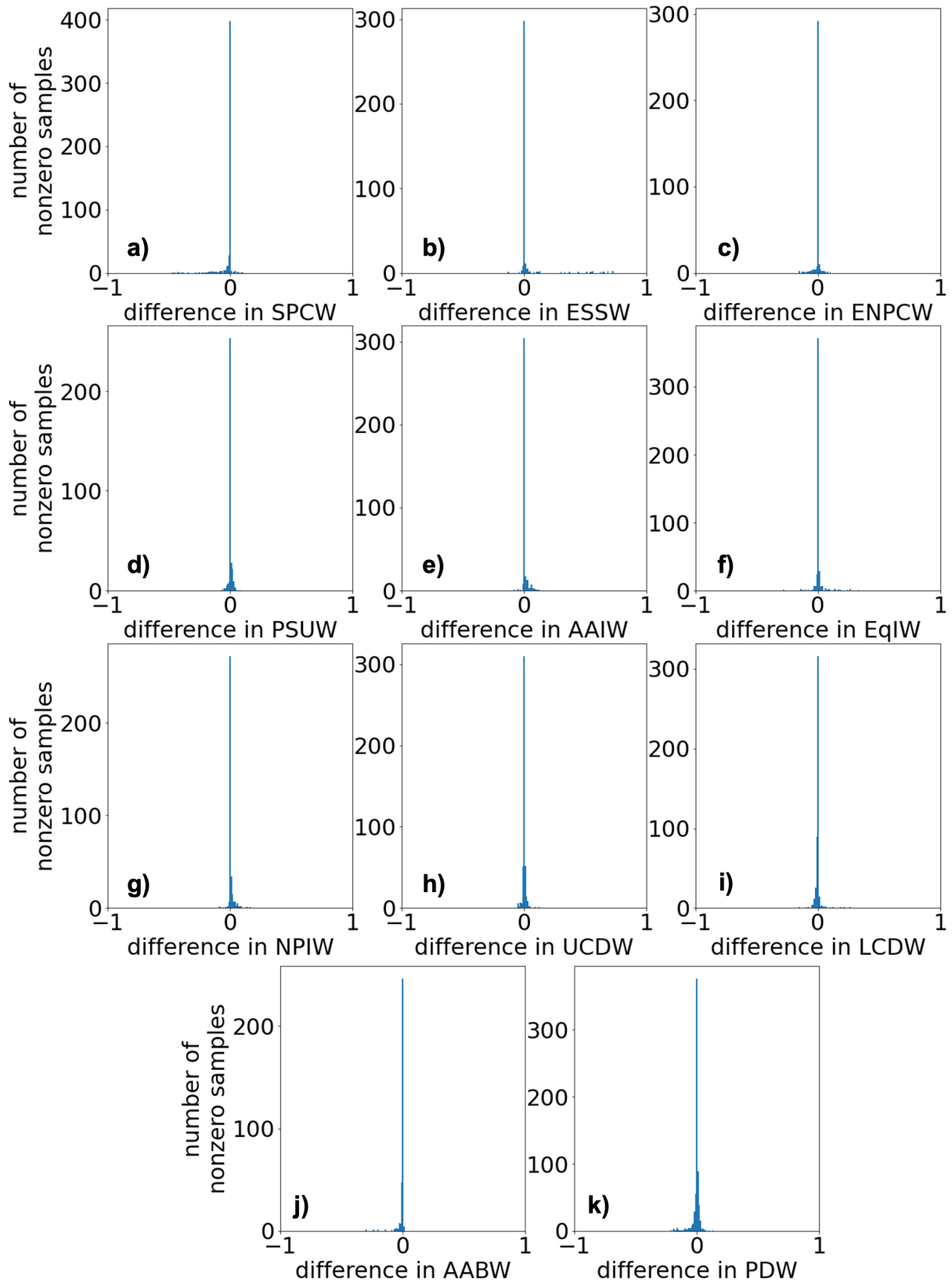
Once the spline is fit, we can compute the predicted property values according to the spline at each potential density increment, and use this to define our end-members for the increment.

**Figure S1.** Comparison of parameter weighting in thermocline water masses. The x-axis is the difference between the GP15 water mass fractions resulting from our thermocline

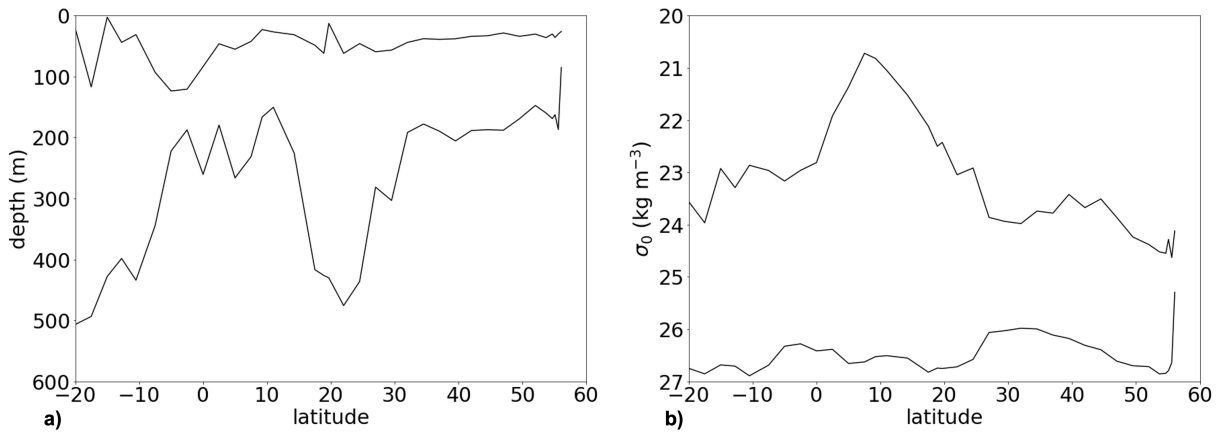
water mass weighting and from (Peters et al., 2018)'s cited weights. The y-axis is the number of GP15 samples with water mass fractions above zero in at least one set of results from the two weighting schemes. In other words, samples that had a water mass fraction of zero in both of the weighting schemes were excluded from the histogram to focus on the relevant samples from the thermocline. Bins sizes are approximately 0.01 (e.g. the bin including zero is from approximately -0.005 to 0.005).



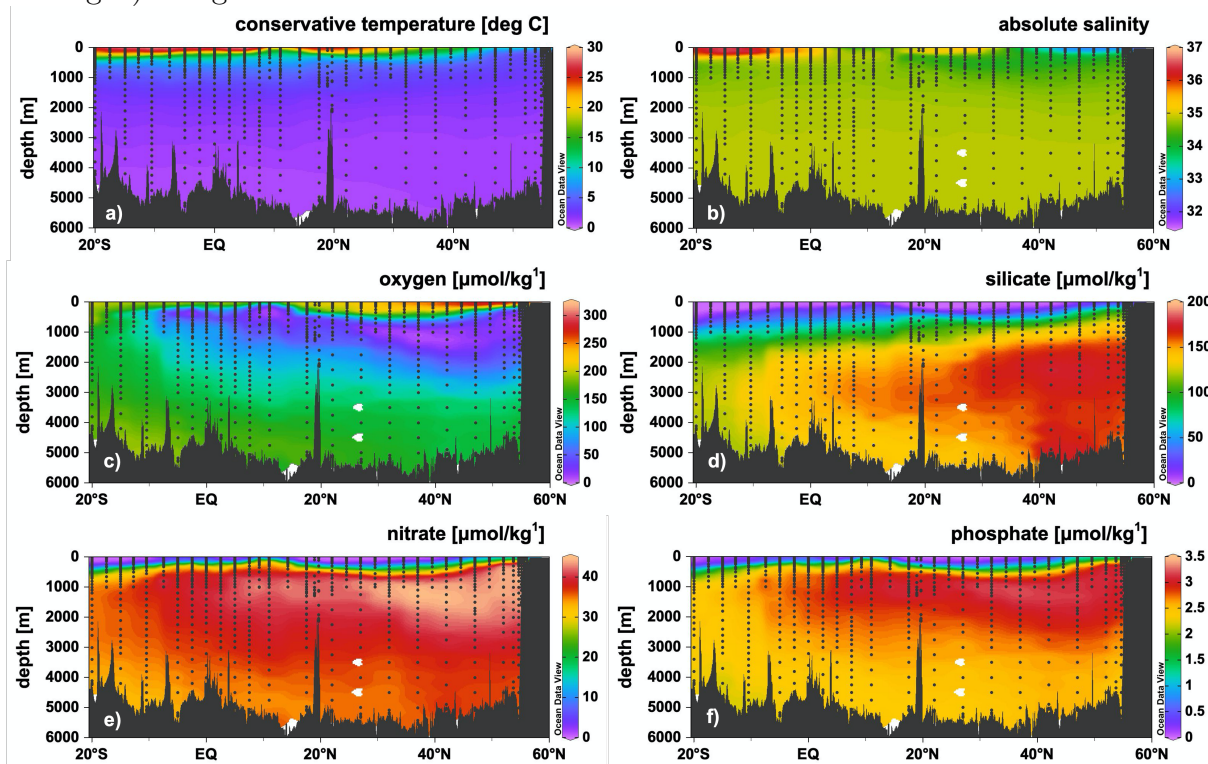
**Figure S2.** Comparison of parameter weighting in the intermediate and deep water. The x-axis is the difference between the GP15 water mass fractions resulting from our intermediate and deep water mass weighting and from (Peters et al., 2018)'s cited weights. The y-axis is the number of GP15 samples showing a given difference between the two weighting schemes. The y-axis is the number of GP15 samples with water mass fractions above zero in at least one set of results from the two weighting schemes. In other words, samples that has a water mass fraction of zero from both of the weighting schemes were excluded from the histogram to focus on the relevant intermediate and deep water samples. Bins sizes are approximately 0.01 (e.g. the bin including zero is from approximately -0.005 to 0.005).



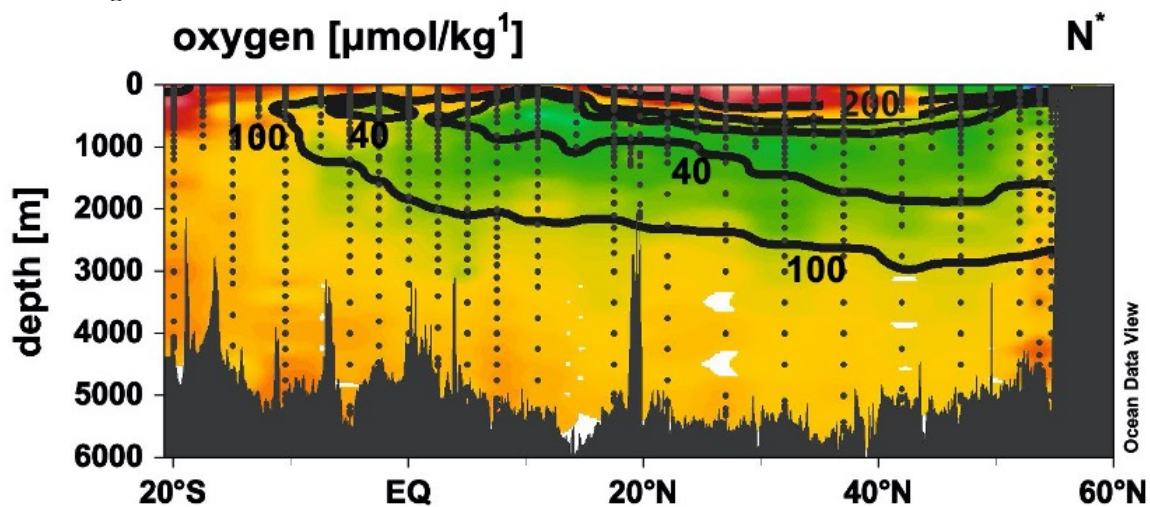
**Figure S3.** Thermocline a) depth and b) potential density anomaly ( $\sigma_0$ ) boundaries for each GP15 station.



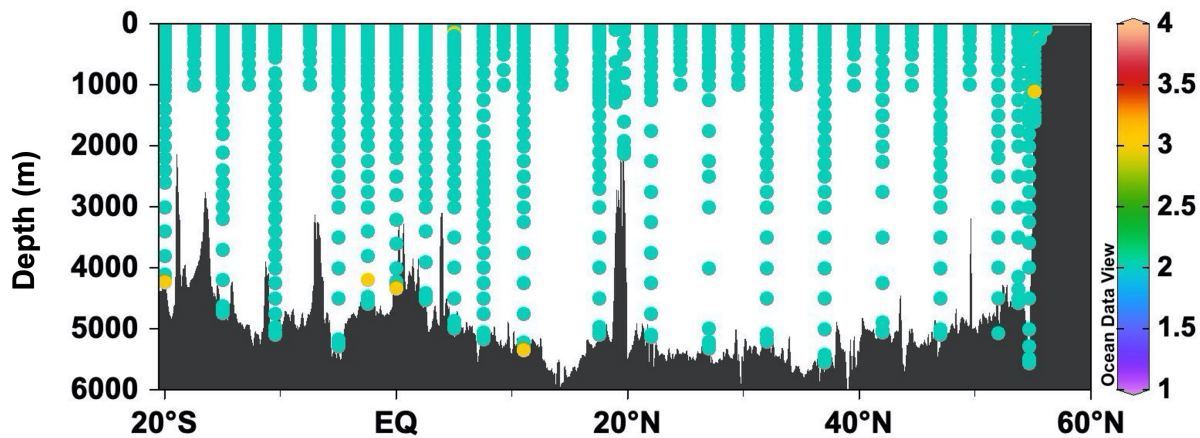
**Figure S4.** Full water column section plots of a) conservative temperature ( $^{\circ}\text{C}$ ), b) absolute salinity, c) dissolved oxygen concentrations ( $\mu\text{mol kg}^{-1}$ ), d) silicate concentrations ( $\mu\text{mol kg}^{-1}$ ), e) nitrate concentrations ( $\mu\text{mol kg}^{-1}$ ), and f) phosphate concentrations ( $\mu\text{mol kg}^{-1}$ ) along the GP15 transect.



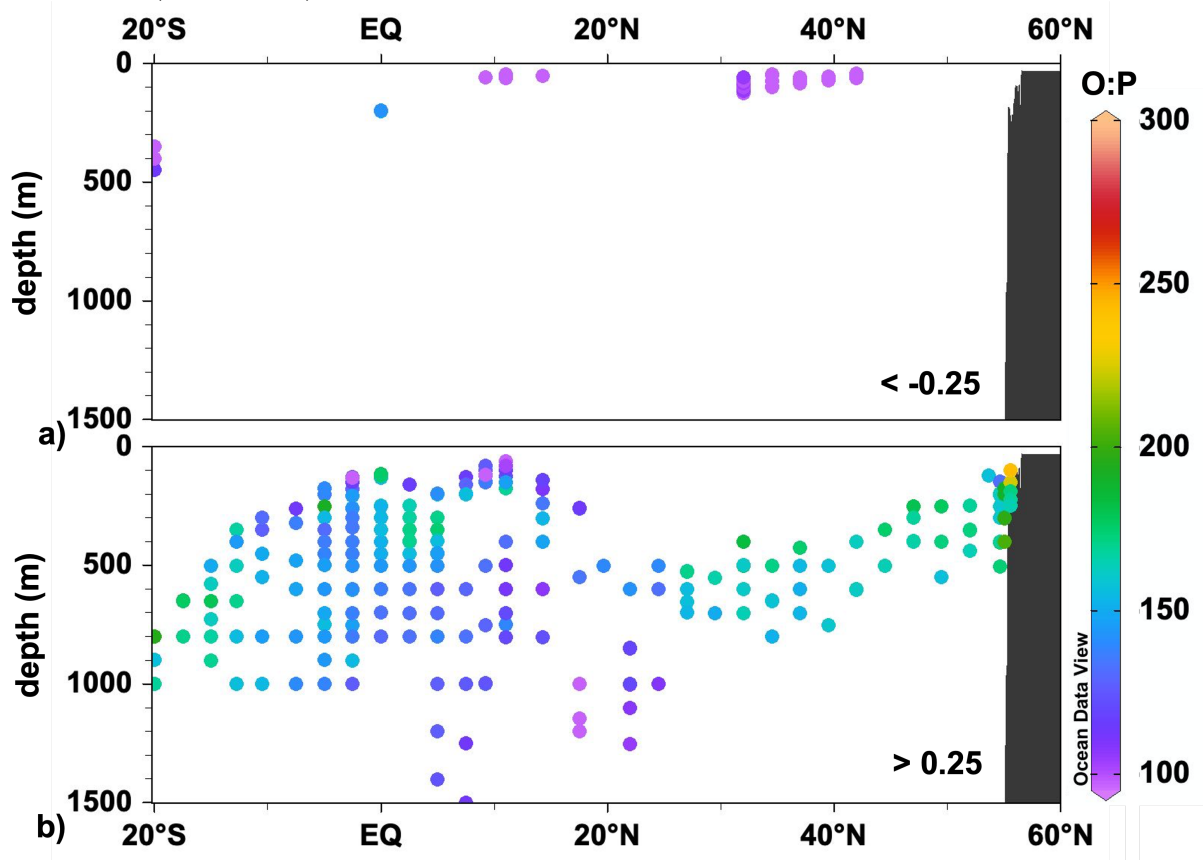
**Figure S5.**  $N^*$  ( $\mu\text{mol kg}^{-1}$ ) with dissolved oxygen ( $\mu\text{mol kg}^{-1}$ ) contours in the full water column along the GP15 transect.



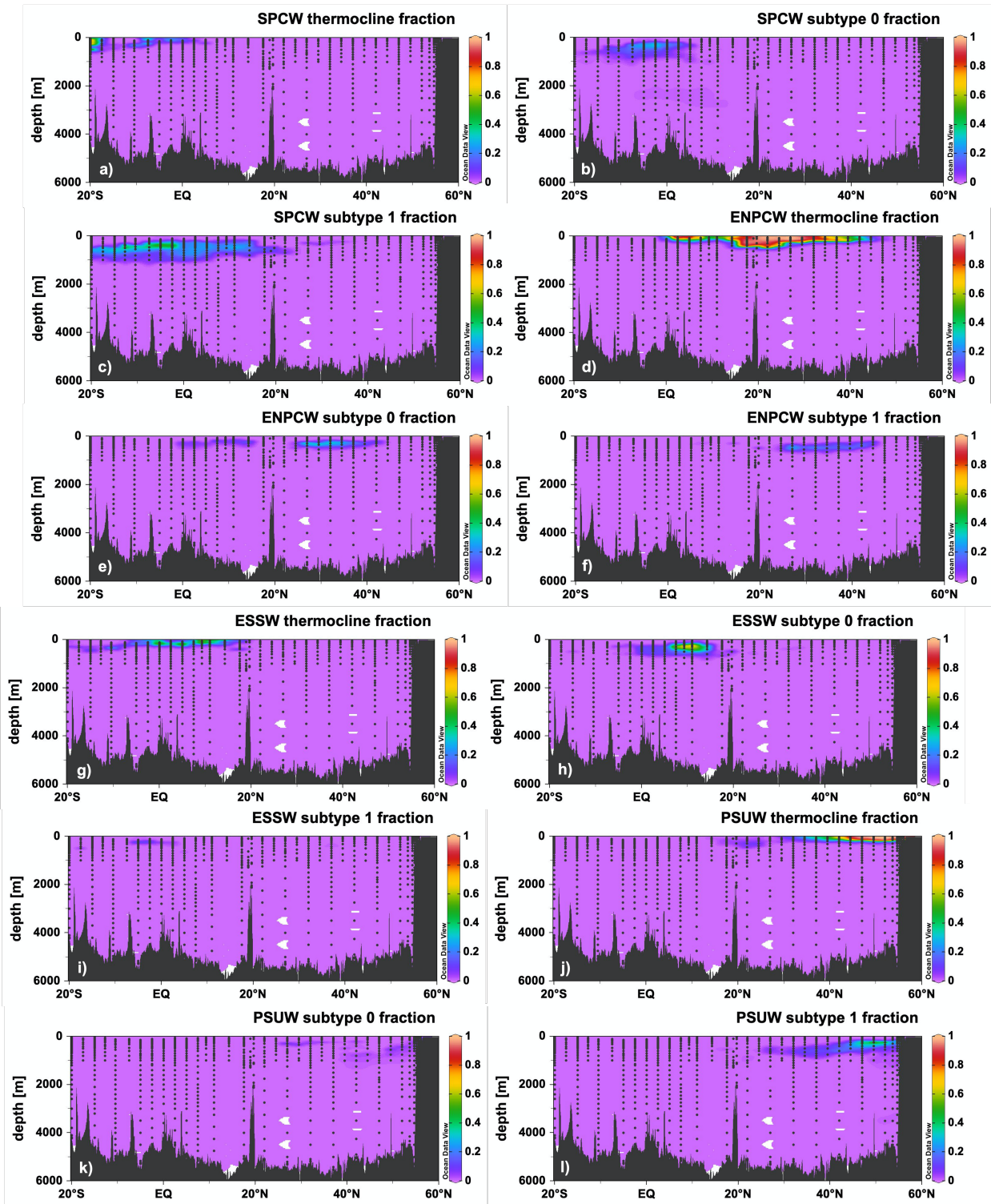
**Figure S6.** The yellow dots show nitrate and phosphate data flagged as probably bad (3) compared to most of the data in teal flagged as probably good (2). No data flagged as a known bad value (4) was included in the OMP analysis.



**Figure S7.** The algorithm-chosen O:P ratio ( $\mu\text{mol}/\mu\text{mol}$ ) along the GP15 transect where a) phosphate assimilation is more than  $-0.25$  ( $\mu\text{mol kg}^{-1}$ ) and b) phosphate regeneration is above  $0.25$  ( $\mu\text{mol kg}^{-1}$ ).



**Figure S8.** Water mass fractions for water mass subtypes. For the thermocline water masses included in the intermediate and deep analysis, water mass fractions for the thermocline analysis are provided in addition to subtypes. AABW and UCDW are not included as these only have one defined archetype (Table S1). SPSTSW is not included as this water mass was only included in the thermocline analysis. The colorbar represents the water mass fractions for SPCW (a-c), ENPCW (d-f), ESSW (g-i), PSUW (j-l), AAIW (m-n), EqIW (o-p), LCDW (q-r), NPIW (s-u), and PDW (v-x).



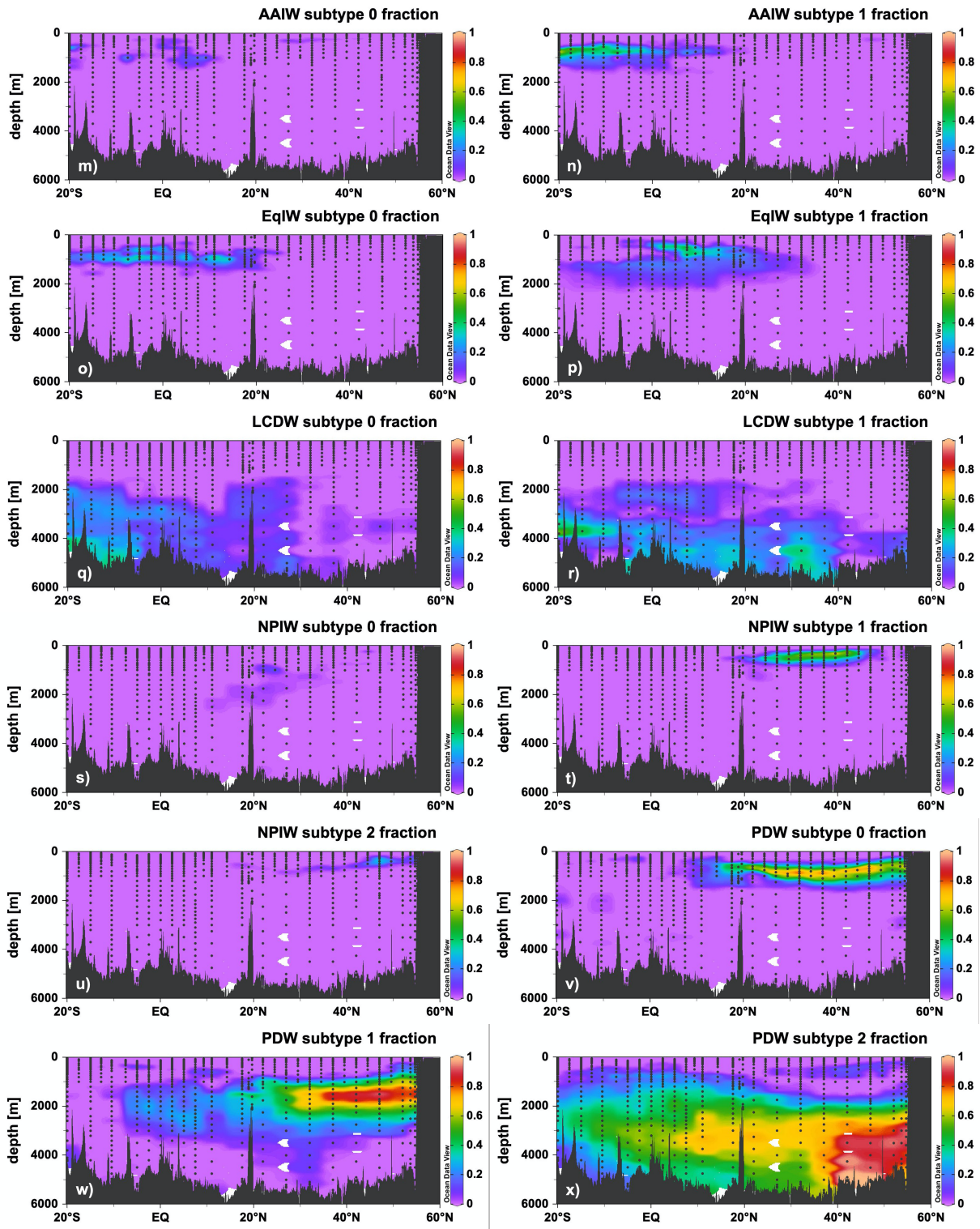


**Figure S9.** Profiles of a) oxygen ( $\mu\text{mol kg}^{-1}$ ) and b) nitrate ( $\mu\text{mol kg}^{-1}$ ) for GP15 Station 39, located at  $20^\circ\text{S}$ . The oxygen minimum and nitrate maximum characteristic of Upper Circumpolar Deep Water (UCDW) align between 1000 m and 2000 m, where our water mass analysis yielded the highest UCDW mass fractions.

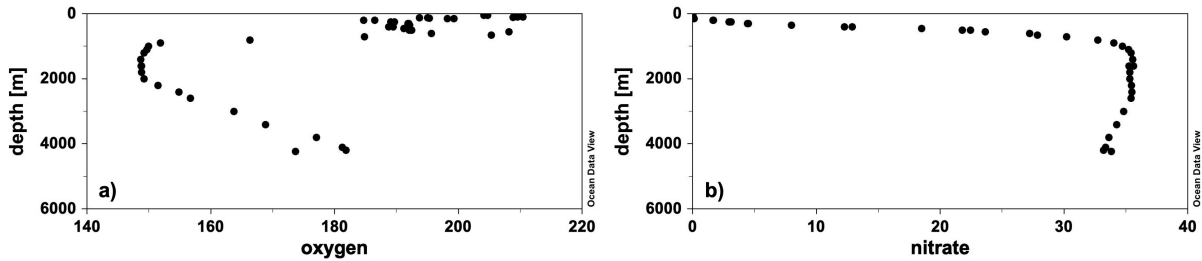


**Figure S10.** Lower Circumpolar Deep Water (LCDW) fraction with  $\sigma_4$  contours 45.84 and 45.88  $\text{kg m}^{-3}$  overlain as black lines. Figure 10.18 of Talley (2011) places LCDW below 45.84  $\text{kg m}^{-3}$  at  $28^\circ\text{S}$  and 45.88  $\text{kg m}^{-3}$  at  $24^\circ\text{N}$ . In our analysis, LCDW water mass fractions were primarily below the depths of these contour lines, in agreement with Talley (2011).

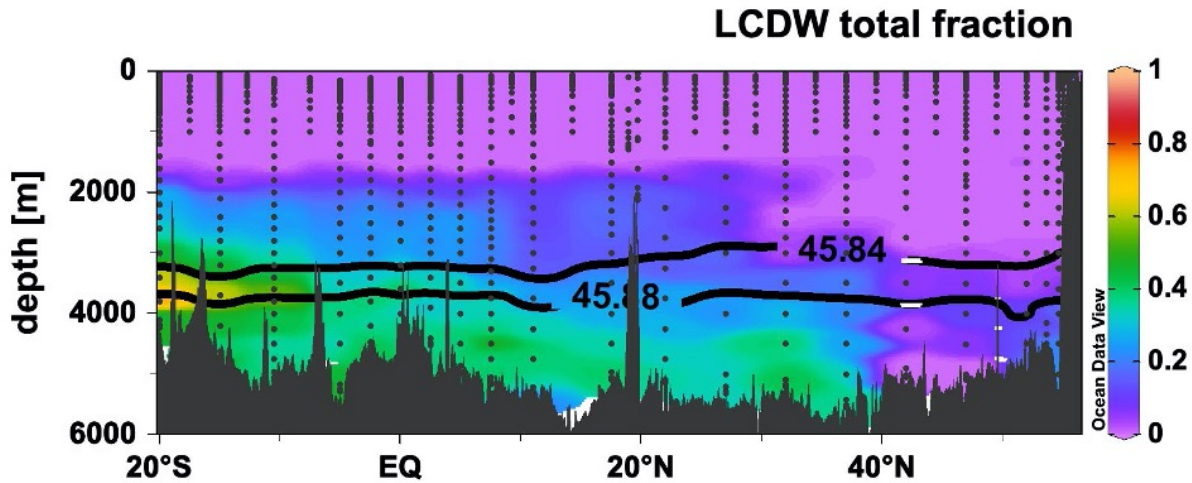


**Figure S11.** Histograms of a) temperature ( $^{\circ}\text{C}$ ) b) absolute salinity, c) oxygen ( $\mu\text{mol kg}^{-1}$ ), d) silicate ( $\mu\text{mol kg}^{-1}$ ), e) nitrate ( $\mu\text{mol kg}^{-1}$ ), and f) phosphate ( $\mu\text{mol kg}^{-1}$ ) residuals for all samples in the thermocline and intermediate and deep water analyses.

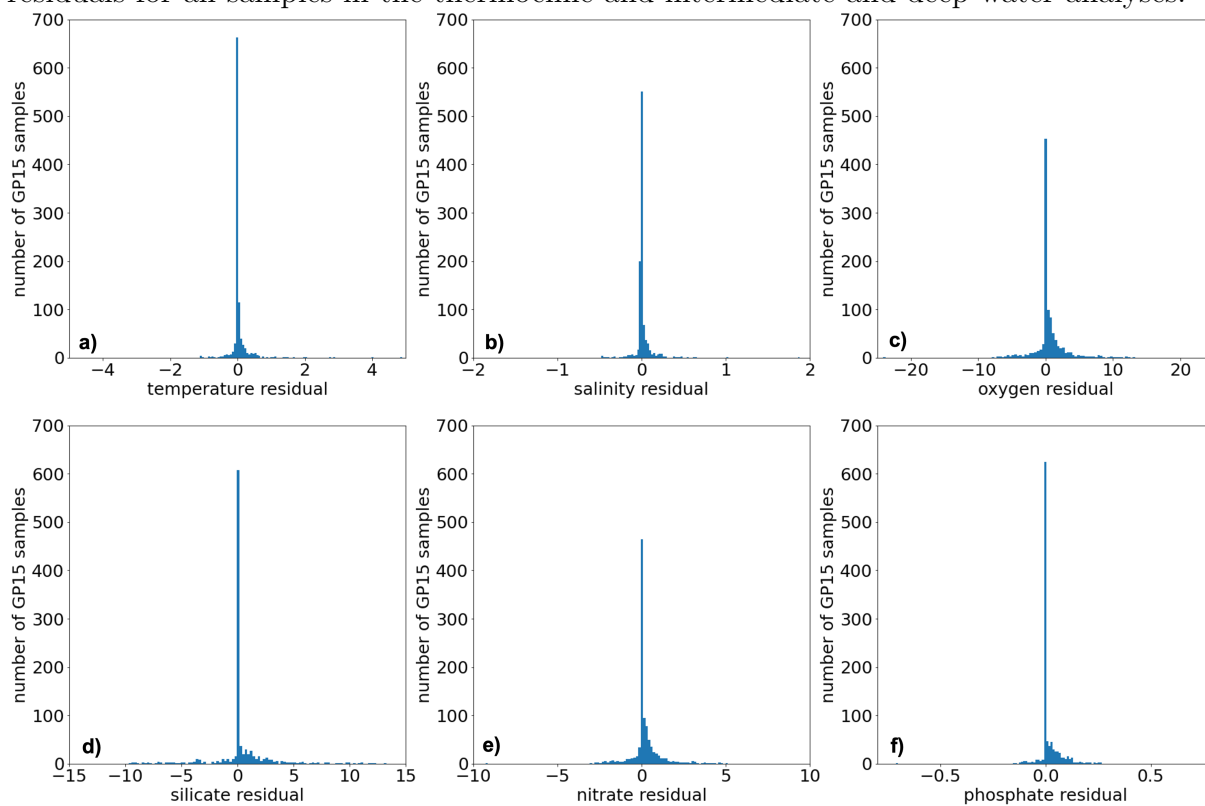


**Figure S12.** Range in residuals compared with previous studies for a) temperature ( $^{\circ}\text{C}$ ) b) absolute salinity, c) oxygen ( $\mu\text{mol kg}^{-1}$ ), d) silicate ( $\mu\text{mol kg}^{-1}$ ), e) nitrate ( $\mu\text{mol kg}^{-1}$ ), and f) phosphate ( $\mu\text{mol kg}^{-1}$ ).

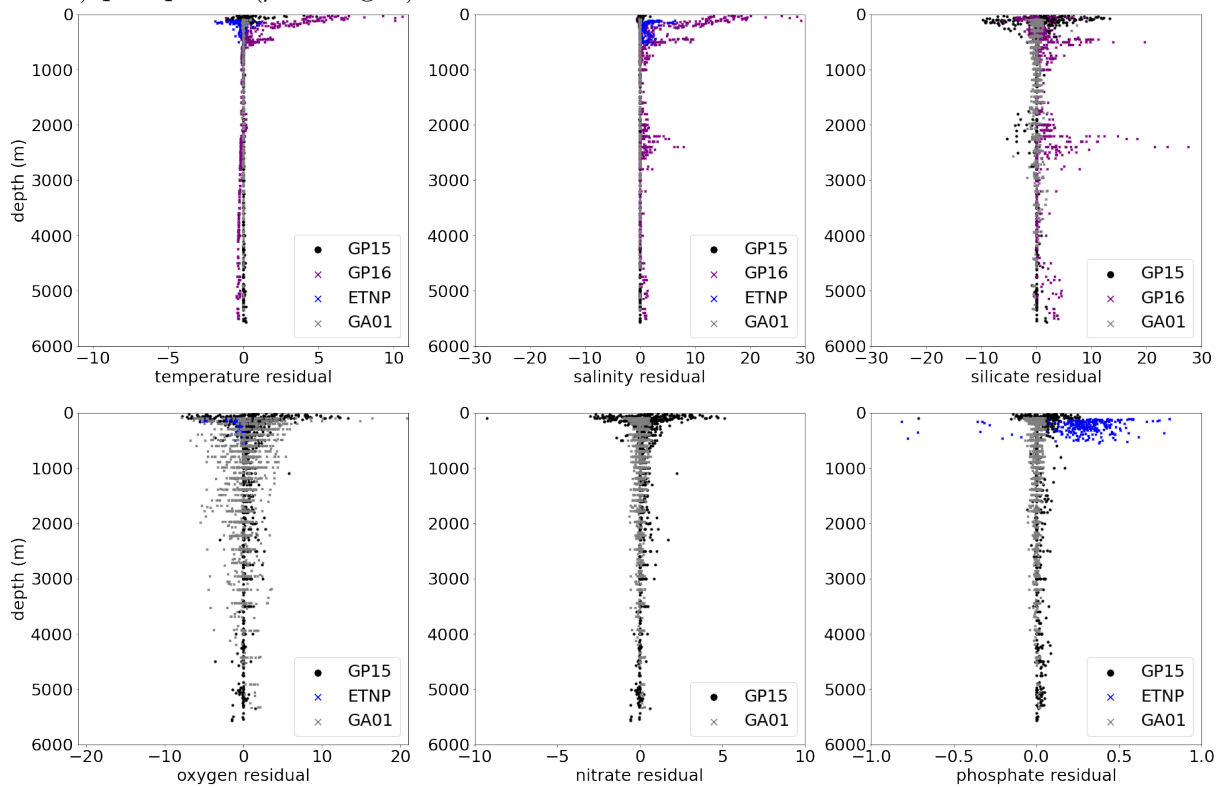


**Figure S13.** The standard deviation of residuals with altered parameter weightings for a) conservative temperature ( $^{\circ}\text{C}$ ) b) absolute salinity, c) oxygen ( $\mu\text{mol kg}^{-1}$ ), d) silicate ( $\mu\text{mol kg}^{-1}$ ), e) nitrate ( $\mu\text{mol kg}^{-1}$ ), and f) phosphate ( $\mu\text{mol kg}^{-1}$ ).

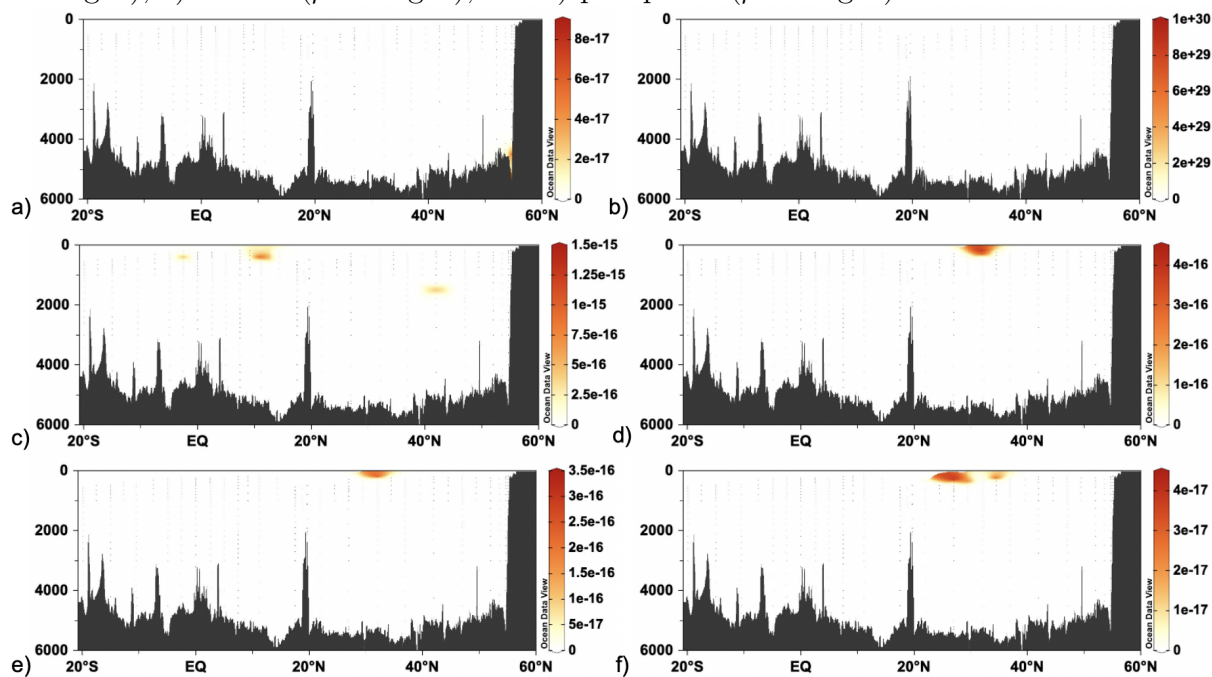


**Figure S14.** Thermocline endmember properties for a) conservative temperature ( $^{\circ}\text{C}$ ) b) absolute salinity, c) oxygen ( $\mu\text{mol kg}^{-1}$ ), d) silicate ( $\mu\text{mol kg}^{-1}$ ), e) nitrate ( $\mu\text{mol kg}^{-1}$ ), and f) phosphate ( $\mu\text{mol kg}^{-1}$ ).

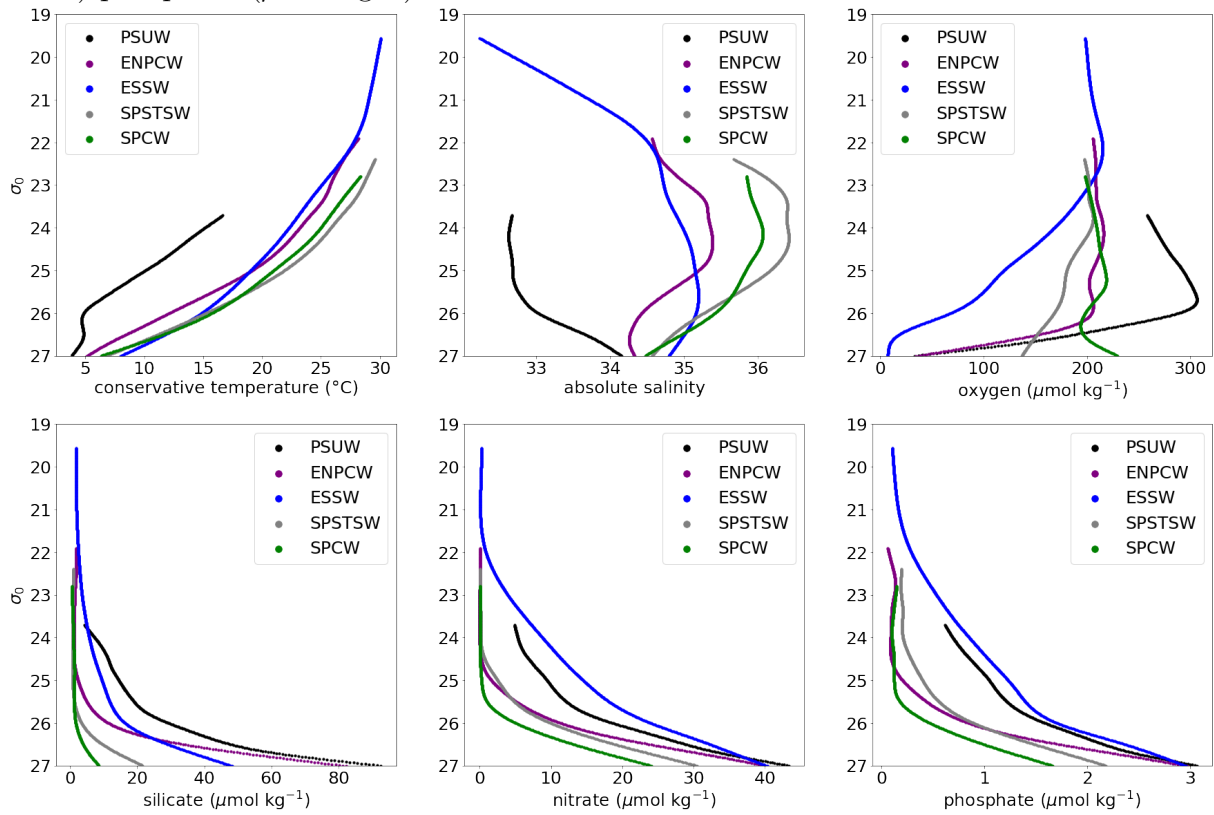


**Figure S15.** Approximate density range we would expect to find NPCMW. This intersects with several different thermocline and intermediate water types present in our analysis.

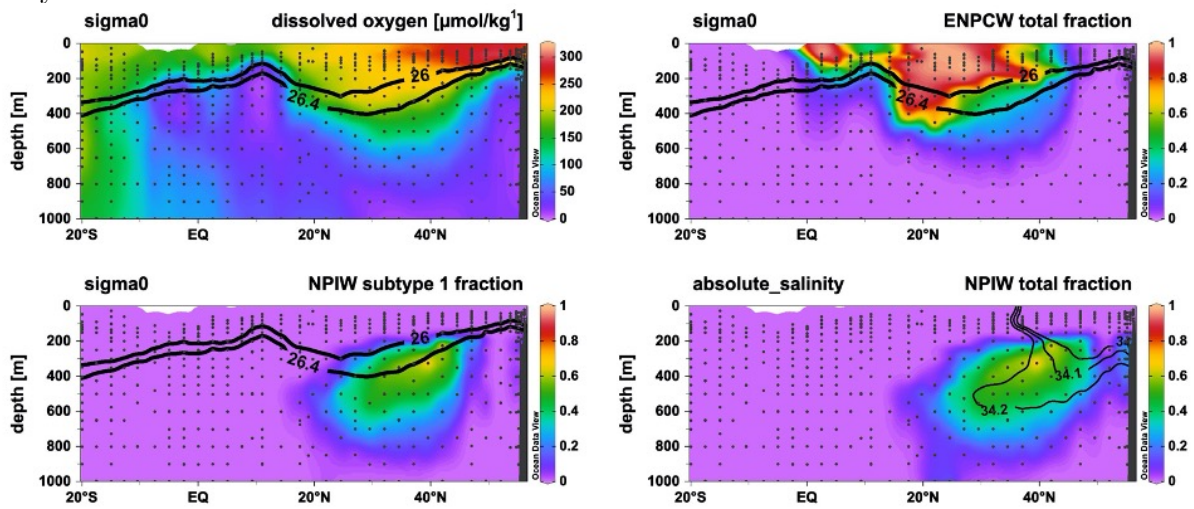


**Figure S16.** SPCW carries the signal of the Eastern Tropical South Pacific (Peruvian) oxygen deficient zone as shown by the dissolved oxygen contour of  $50 \mu\text{mol kg}^{-1}$ .

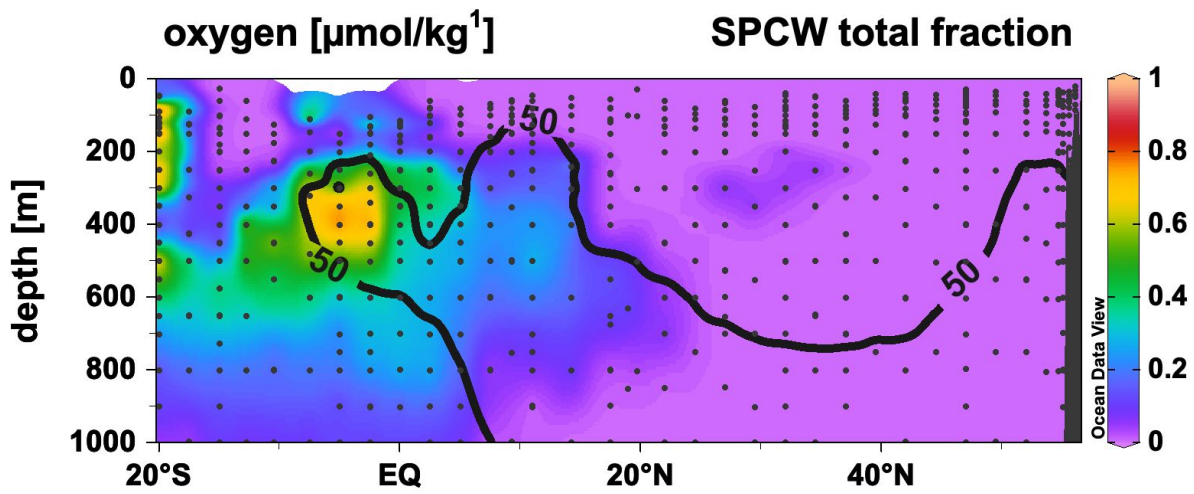


Figure S17. ESSW carries the signal of the Eastern Tropical North Pacific oxygen deficient zone as shown by the dissolved oxygen contour of  $50 \mu\text{mol kg}^{-1}$ .

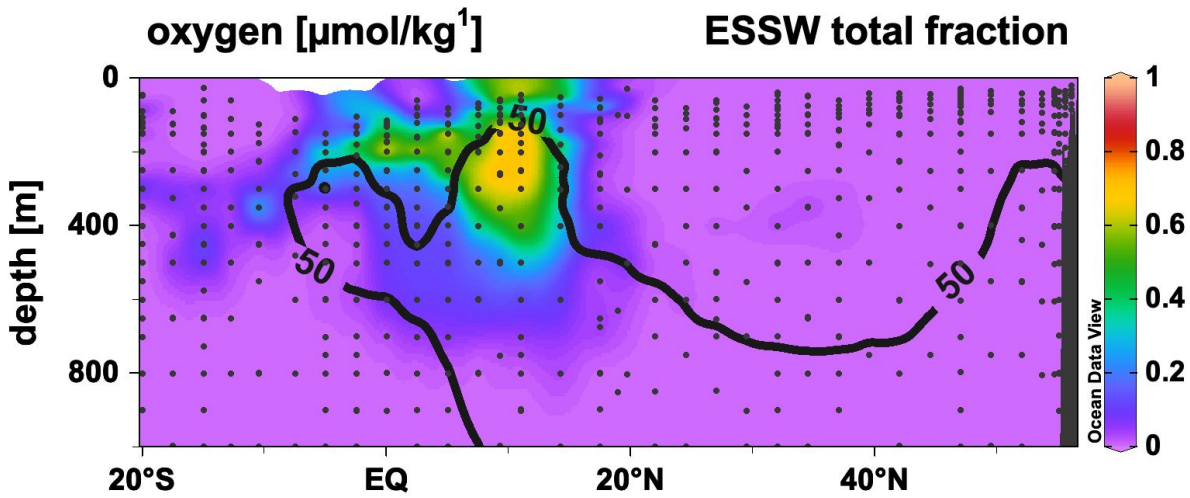
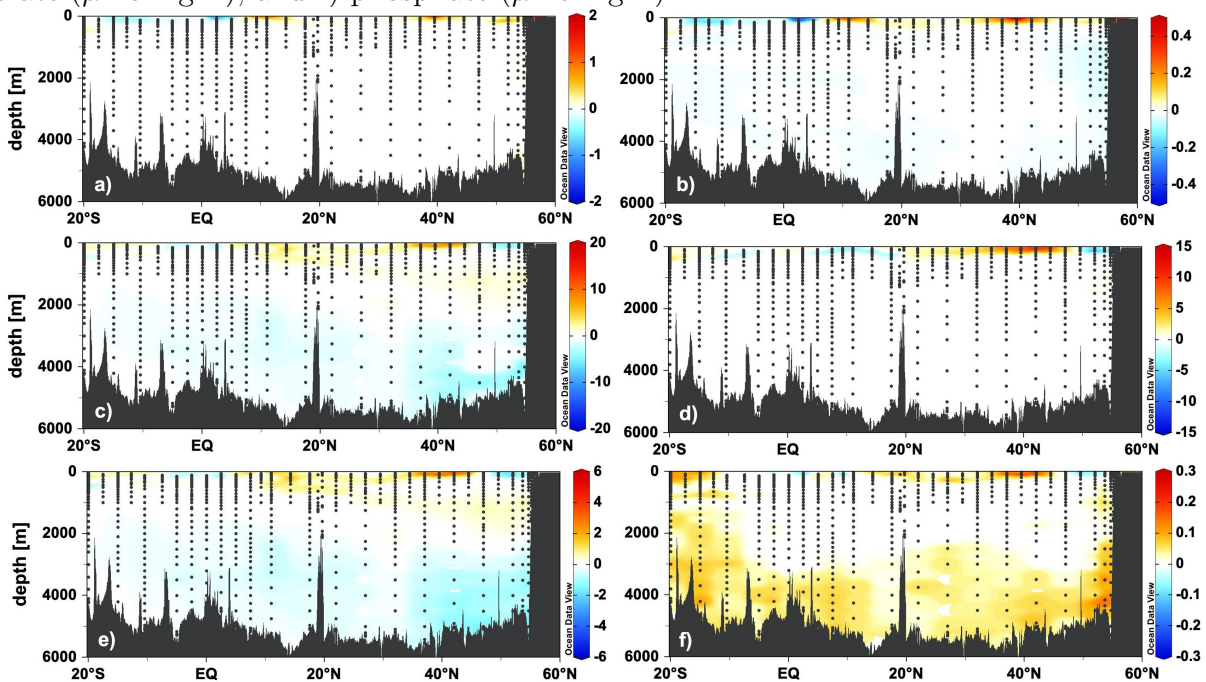
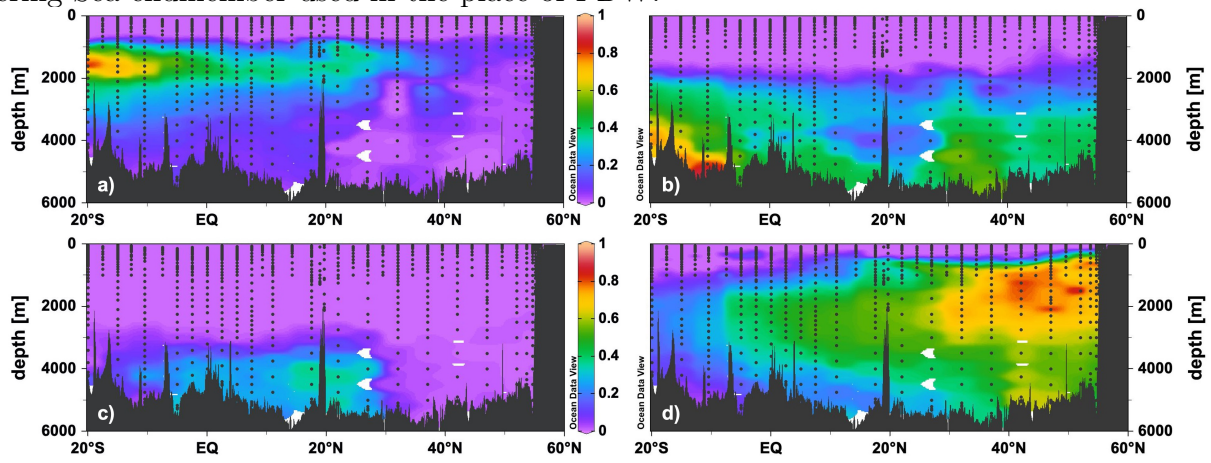


Figure S18. Residuals for the OMP using the Bering Sea endmember a) Conservative temperature ( $^{\circ}\text{C}$ ) b) absolute salinity, c) oxygen ( $\mu\text{mol kg}^{-1}$ ), d) silicate ( $\mu\text{mol kg}^{-1}$ ), e) nitrate ( $\mu\text{mol kg}^{-1}$ ), and f) phosphate ( $\mu\text{mol kg}^{-1}$ ).



**Figure S19.** The water mass fractions of a) UCDW b) LCDW, c) AABW, and d) the Bering Sea endmember used in the place of PDW.



**Table S1.** Water mass subtype definitions. Each line defines the properties of a water mass subtype (archetype). Subtypes are numbered beginning with '0'.

Water mass	Temperature (°C)	Salinity (S)	Silicate ( $\mu\text{mol kg}^{-1}$ )	Nitrate ( $\mu\text{mol kg}^{-1}$ )	Phosphate ( $\mu\text{mol kg}^{-1}$ )	Oxygen ( $\mu\text{mol kg}^{-1}$ )
AABW 0	0.07	34.87	128.23	32.46	2.26	216.23
AAIW 0	5.04	34.39	11.51	23.99	1.67	272.31
AAIW 1	4.47	34.40	20.43	28.54	1.99	231.45
ENPCW 0	15.99	34.80	3.54	3.51	0.32	213.72
ENPCW 1	8.55	34.20	28.66	21.55	1.57	177.51
EqIW 0	5.46	34.73	72.17	42.52	3.07	42.82
EqIW 1	8.74	34.84	44.15	38.85	2.86	8.04
LCDW 0	1.55	34.90	93.37	31.50	2.18	190.11
LCDW 1	0.77	34.86	119.83	32.43	2.26	199.11
NPIW 0	9.41	34.34	32.63	19.84	1.41	177.00
NPIW 1	7.15	34.02	25.26	15.05	1.19	268.40
NPIW 2	4.54	34.12	77.91	34.76	2.52	114.14
PDW 0	3.74	34.43	117.45	43.87	3.16	11.38
PDW 1	2.16	34.71	167.51	44.57	3.15	23.94
PDW 2	1.20	34.87	171.60	37.10	2.59	136.80
PSUW 0	6.13	32.71	19.72	11.96	1.21	324.84
PSUW 1	4.43	33.60	50.07	29.99	2.28	178.86
SPCW 0	18.62	35.68	0.76	1.04	0.18	206.65
SPCW 1	8.40	34.62	6.47	19.98	1.43	201.51
UCDW 0	2.50	34.73	83.32	34.11	2.39	168.79

**Table S2.** Comparison of our AAIW endmember properties with those from SAMW endmembers used by Holte, Talley, Chereskin, and Sloyan (2013). Note Holte et al. (2013) report potential temperature and practical salinity while we report conservative temperature and absolute salinity.

Water mass	temperature (°C)	salinity (S)	Nitrate ( $\mu\text{mol kg}^{-1}$ )	Phosphate ( $\mu\text{mol kg}^{-1}$ )	Oxygen ( $\mu\text{mol kg}^{-1}$ )	Silicate ( $\mu\text{mol kg}^{-1}$ )
AAIW 0	5.04	34.39	23.99	1.67	272.31	11.51
AAIW 1	4.47	34.40	28.54	1.99	231.45	20.43
SAMW (27.0-27.1 $\sigma_0$ )	5.30	34.23	25.0	1.7	255	10.7
SAMW (27.1-27.2 $\sigma_0$ )	4.48	34.26	29.1	2.0	226	21.7

..

## References

- Cutter, G. A., Casciotti, K. L., & Lam, P. J. (2018). US GEOTRACES Pacific meridional transect–GP15 cruise report.
- GEOTRACES. (n.d.). *GEOTRACES quality flag policy*.  
<https://www.geotraces.org/geotraces-quality-flag-policy/>.
- Holte, J. W., Talley, L. D., Chereskin, T. K., & Sloyan, B. M. (2013). Subantarctic mode water in the southeast Pacific: Effect of exchange across the Subantarctic Front. *Journal of Geophysical Research: Oceans*, *118*(4), 2052–2066.
- Jenkins, W., Smethie Jr, W., Boyle, E., & Cutter, G. (2015). Water mass analysis for the US GEOTRACES (GA03) North Atlantic sections. *Deep Sea Research Part II: Topical Studies in Oceanography*, *116*, 6–20.
- Peters, B. D., Jenkins, W. J., Swift, J. H., German, C. R., Moffett, J. W., Cutter, G. A., ... Casciotti, K. L. (2018). Water mass analysis of the 2013 US GEOTRACES eastern Pacific zonal transect (GP16). *Marine Chemistry*, *201*, 6–19.
- SeaDataNet. (2010, May). Data quality control procedures (2.0 ed.) [Computer software manual].
- Talley, L. D. (2011). *Descriptive physical oceanography: An introduction*. Academic Press.